



Cinobufotalin powerfully reversed EBV-miR-BART22-induced cisplatin resistance via stimulating *MAP2K4* to antagonize non-muscle myosin heavy chain IIA/glycogen synthase 3 β / *β -catenin* signaling pathway

Yiyi Liu^{a,1}, Qingping Jiang^{b,c,1}, Xiong Liu^{b,d,1}, Xian Lin^{a,1}, ZiBo Tang^a, Chen Liu^a, Jin Zhou^a, Mengyang Zhao^a, Xin Li^e, Zhao Cheng^{e,f}, Libo Li^a, Yingying Xie^a, Zhen Liu^{a,g,**}, Weiyi Fang^{a,*}

^a Cancer Center, Integrated Hospital of Traditional Chinese Medicine, Southern Medical University, Guangzhou, China

^b Cancer Institute, School of Basic Medical Science, Southern Medical University, Guangzhou, China

^c Department of Pathology, Third Affiliated Hospital, Guangzhou Medical University, Guangzhou, China

^d Department of Otolaryngology, Head and Neck Surgery, Nanfang Hospital, Southern Medical University, Guangzhou, Guangdong, People's Republic of China

^e Shenzhen Key Laboratory of Viral Oncology, the Clinical Innovation & Research Center (CIRC), Shenzhen Hospital, Southern Medical University, Shenzhen, China

^f Department of Pediatric Otorhinolaryngology, Zhujiang Hospital, Southern Medical University, Guangzhou, China

^g Key Laboratory of Protein Modification and Degradation, School of Basic Medical Sciences, Affiliated Cancer Hospital and Institute of Guangzhou Medical University, Guangzhou, China

ARTICLE INFO

Article history:

Received 15 January 2019

Revised 16 August 2019

Accepted 19 August 2019

Available online 5 October 2019

Keywords:

EBV-miR-BART22

Cinobufotalin

DDP chemoresistance

Stemness

NPC

ABSTRACT

Background: Nasopharyngeal carcinoma (NPC) is an Epstein-Barr virus (EBV)-related tumor. The role of EBV-encoding miR-BART22 is still unclear in NPC. This study aimed to identify the detailed mechanisms by which EBV-miR-BART22 functions as a tumor-promoting factor and evaluate the action of cinobufotalin in treating EBV-miR-BART22-overexpressing NPC cells.

Methods: Using real-time PCR, western blotting, immunohistochemistry, and In situ hybridization, we detected the expression of miR-BART22 and MAP2K4 in tissues and cells, as well as evaluated their clinical relevance in NPC patients. The effects of miR-BART22 on cell metastasis, stemness and DDP chemoresistance were examined by sphere formation assay, side population analysis, transwell, boyden, in vivo xenograft tumor mouse model et al. Western blotting, immunofluorescence staining, luciferase reporter assay, ChIP, EMSA and Co-IP assay et al. were performed to explore the detailed molecular mechanism of EBV-miR-BART22 in NPC. Finally, we estimated the effects and molecular basis of Cinobufotalin on EBV-miR-BART22-overexpressing NPC cells in vitro and in vivo assays.

Findings: We observed that EBV-miR-BART22 not only promoted tumor stemness and metastasis, but also enhanced the resistance to Cisplatin (DDP) in vitro and in vivo. Mechanistic analysis indicated that EBV-miR-BART22 directly targeted the *MAP2K4* and upregulated non-muscle myosin heavy chain IIA (*MYH9*) expression by *PI3K/AKT/c-Jun*-induced transcription. Further, *MYH9* interacted with glycogen synthase 3 β (*GSK3 β*) protein and induced its ubiquitin degradation by activating *PI3K/AKT/c-Jun*-induced *ubiquitin* transcription and the latter combined with increased TRAF6 E3 ligase, which further bound to *GSK3 β* protein. Reductions in the *GSK3 β* protein thus promoted *β -catenin* expression and nuclear translocation, which induced tumor stemness and the epithelial-to-mesenchymal transition (EMT) signals. Furthermore, we observed that cinobufotalin, a new chemically synthesized compound, significantly suppressed EBV-miR-BART22-induced DDP chemoresistance by upregulating *MAP2K4* to suppress *MYH9/GSK3 β / β -catenin* and its downstream tumor stemness and EMT signals in NPC. Finally, clinical data revealed that increased miR-BART22 and reduced *MAP2K4* expression caused the poor prognoses of NPC patients.

Abbreviations: ChIP, Chromatin immunoprecipitation; IHC, Immunohistochemical; qRT-PCR, Quantitative real time polymerase chain reaction; RIP, RNA immunoprecipitation; NPC, Nasopharyngeal carcinoma; EBV, Epstein-Barr virus; EMSA, Electrophoretic mobility shift assay; MTT, 3-(4,5-dimethyl-2-thiazolyl)-2, 5-diphenyl-2H-tetrazolium bromide;; Co-IP, Co-immunoprecipitation; EMT, epithelial-mesenchymal transition; FISH, Fluorescence in situ hybridization; DDP, cisplatin, Cis-diamminedichloroplatinum; BARTs, BamHI A rightward transcripts; *MAP2K4*, mitogen-activated protein kinase kinase 4; *MYH9*, non-muscle myosin heavy chain IIA; *GSK3 β* , glycogen synthase 3 β .

* Corresponding author.

** Corresponding author at: Cancer Center, Integrated Hospital of Traditional Chinese Medicine, Southern Medical University, Guangzhou, China.

E-mail addresses: Narcissus.jane@163.com (Z. Liu), fangweiyi1975@163.com (W. Fang).

¹ These authors contribute to the equal work.

<https://doi.org/10.1016/j.ebiom.2019.08.040>

2352-3964/© 2019 The Authors. Published by Elsevier B.V. This is an open access article under the CC BY-NC-ND license. (<http://creativecommons.org/licenses/by-nc-nd/4.0/>)

Interpretation: Our study provides a novel mechanism that cinobufotalin reversed the DDP chemoresistance and EMT induced by EBV-miR-BART22 in NPC.

© 2019 The Authors. Published by Elsevier B.V.
This is an open access article under the CC BY-NC-ND license.
(<http://creativecommons.org/licenses/by-nc-nd/4.0/>)

Research in context

Evidence before this study

Infection with the Epstein-Barr virus (EBV) is a strong predisposing factor in the development of nasopharyngeal carcinoma (NPC). Previously, EBV-miR-BART22 has been found highly expressed in NPC tissues. However, how the NPC-associated EBV miRNA precisely regulate the tumor progression and chemoresistance remains obscure in NPC.

Added value of this study

This study identifies EBV-miR-BART22 as an oncogene that promotes tumor stemness, metastasis and DDP chemotherapy resistance in NPC. The role and detailed molecular basis of EBV-miR-BART22 was examined by transwell, boyden, sphere formation assay, western blotting and mouse xenograft tumor model et al. The expression levels of EBV-miR-BART22 and its targeted gene mitogen-activated protein kinase kinase 4 (*MAP2K4*) were evaluated in NPC and nasopharynx tissues. EBV-miR-BART22 expression was negatively correlated with *MAP2K4* protein expression in NPC tissues, and NPC patients with high miR-BART22 and low *MAP2K4* protein expression showed the worst survival prognosis. Furthermore, we found that EBV-miR-BART22 targets *MAP2K4* and further stimulates *MYH9*-mediated *GSK3 β* ubiquitin protein degradation, which thus activates β -*catenin* and its downstream tumor stemness and EMT signaling pathways. Finally, the anti-tumor activity of cinobufotalin in reversing EBV-miR-BART22-induced DDP chemoresistance was shown by inducing *MAP2K4* to antagonize *MYH9/GSK3 β / β -catenin* signaling pathway in NPC.

Implications of all the available evidence

Together, our study not only highlights the key role of EBV-miR-BART-22 in the pathogenesis of NPC, but also demonstrates the significance of cinobufotalin in reversing EBV-miR-BART-22-stimulated DDP chemoresistance in NPC.

1. Introduction

NPC is endemic in Southern China and Southeast Asia with high incidences seen [1,2]. It is a malignant tumor that is characterized by a high rate of local invasion and early, distant metastases in the nasopharynx [3,4]. In previous studies, nasopharynx carcinogenesis had been shown to be closely related to EBV infection [5,6]. As a human herpesvirus 4 (HHV4) family member, EBV establishes a life-long and latent infection in >90% of the world's population [7–9]. The clinical use of Epstein-Barr virus (EBV) as a surrogate biomarker for population screening, prognostication, and disease surveillance for NPC continues to increase [10,11]. MicroRNA (miRNA) dysregulation plays a vital role during the tumorigenic process [12–14], from initiation and development to progression toward a metastatic phenotype [15]. BamHI A rightward transcripts (BARTs) are particularly abundant in EBV-associated carcinomas and encode a large number of miRNAs [16–18] involved in tu-

mor progression and treatment [19]. For instance, the EBV-encoded miRNA BART1 induces tumor metastases by regulating the PTEN-dependent pathway [20]. EBV-miR-BART7 and BART13 were highly expressed in NPC and served as a poor indicator for NPC prognosis [21]. Previously, we had found that EBV-miR-BART22 expression is higher in NPC tissues compared with those of adjacent mucosal tissues [22,23], which suggested that EBV-miR-BART22 was correlated with NPC pathogenesis. However, the function and molecular basis of EBV-miR-BART22 in NPC has not been reported.

Cancer stem cells (CSCs), a cancer cell subpopulation that can initiate tumorigenesis, exist in many different tumor types. Furthermore, CSCs are the key factors promoting malignant tumor phenotypes including tumor metastasis and chemoresistance [24–28]. However, the mechanisms by which CSCs occur in NPC have not been extensively investigated.

Bufotoxin is toxin found in the white sputum of the Chinese giant salamander, and its main components are resibufogenin (BR), cinobufagin (CB), bufotalin (BT), gamabufotalin (GB), and bufalin [29]. Pharmacologically, bufotoxin has cardiotoxic, anesthetic, detoxifying, pain relieving, reclaiming, and refreshing effects, and is widely used in clinical practice [30]. Recently, it was found that traditional Chinese medicine preparations containing cinobufotalin could inhibit the growth of several different tumor cells, in vitro [31,32]. Clinical observations suggested that cinobufotalin would have inhibitory effects on liver, lung, and pancreatic cancers [33]. However, pre-clinical evaluations of chemically synthesized cinobufotalin have rarely been reported [34]. Furthermore, the difference between the cytotoxicity of cinobufotalin and DDP has never been compared in tumors.

In this study, we performed a more in-depth investigation into the role of EBV-miR-BART22 in NPC pathogenesis and evaluated the action and mechanism of chemically synthesized cinobufotalin in treating EBV-miR-BART22-overexpressing NPC cells. We showed that cinobufotalin is a very promising antitumor agent that powerfully reversed EBV-miR-BART22-induced cisplatin resistance by inducing *MAP2K4* to antagonize *MYH9/GSK3 β / β -catenin*-mediated tumor stemness and EMT signals in NPC.

2. Materials and methods

2.1. Ethical statement

All animal experiments were conducted in accordance with a protocol approved by the Animal Care and Use Committee of Southern Medical University. For the use of these clinical materials for research purpose, written informed consent was obtained from each patient. Approval from the Ethics Committee of the Nanfang Hospital was obtained.

2.2. Cell culture

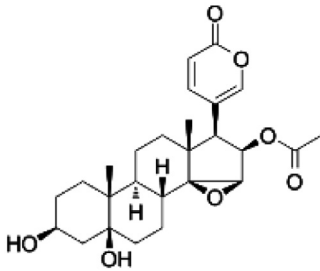
HONE1-EBV⁺ cells were a gift of Dr. S.W. Tsao, the University of Hong Kong. HONE1 and 5-8F cells were stored in the Cancer Research Institute of the Southern Medical University (Guangzhou, China). Both cell lines were cultured in RPMI-1640 (Corning) supplemented with 10% fetal calf serum (Corning) in a humidified chamber with 5% CO₂ at 37°C.

2.3. Clinical samples

Sixty one (61) primary fresh NPC samples with TNM staging and thirty-six [36] non-cancerous fresh nasopharynx(NP) samples as well as one hundred and sixty-three (163) paraffin-embedded NPC cases with clinical prognostic information(55 females and 108 males) and thirty-five [35] paraffin-embedded NP samples were collected from the Nanfang Hospital, Southern Medical University, China, at the time of diagnosis before any therapy.

2.4. Chemicals

Cinobufotalin Chemical Structure:



Cinobufotalin(CB) was purchased from MedChem Express (Monmouth Junction, NJ, USA) (HY-N0880). Stock solutions were prepared using dimethyl sulfoxide (DMSO) (Sigma, St. Louis, MO, USA) as a solvent, and further dissolved to make the desired concentrations for experimental use. MG132 was purchased from Sigma-Aldrich (St. Louis, MO, USA), cycloheximide (CHX) was purchased from Abcam (Cambridge, MA, USA).

2.5. Lentivirus production and infection

Lentiviral particles carrying the hsa-miR-BART22 precursor were constructed by GeneChem (Shanghai, China). HONE1-EBV⁺ and 5-8F cells were infected with lentiviral or control vectors, respectively. Green fluorescent protein was used as a marker to monitor infection efficiency. Overexpression efficiency of miR-BART22 was validated by RT-qPCR.

2.6. RNA isolation, reverse transcription, and RT-qPCR

Total RNA was extracted with the TRIzol reagent (Invitrogen), and complementary DNA (cDNA) was synthesized with the PrimeScript RT reagent Kit (TaKaRa, Dalian, China) according to the manufacturer's instructions. QRT-PCR was performed in triplicate with the SYBR Premix ExTaq (TaKaRa, Dalian, China). We also quantified expression of EBV-miR-BART22 using TaqMan microRNA assays (Applied Biosystems). Briefly, mature miRNAs were reversely transcribed, and qRT-PCR was performed using an All-in-One miRNA qRT-PCR Detection Kit following the manufacturer's protocol (GeneCopoeia). Each primer sequence of the genes used in this study is listed in Supplementary Table 3. The fold changes were calculated by using the 2^{-DDCt} method.

2.7. Transient transfection with mimics, inhibitor or plasmids

SiRNAs for c-Jun, MYH9 and miR-BART22 mimics or its inhibitors were designed and synthesized by RiboBio, Inc. (Guangzhou, China). The sequences and controls are shown in Supplementary Table 4. MAP2K4, MYH9 and GSK3 β plasmids were purchased from Vigenebio Technologies (Shandong, China), and the GSK3 β -K183R plasmids were purchased from Genechem (Shanghai, China). Twelve hours before transfection, HONE1-EBV⁺ and 5-8F

cells were plated into 6-well plates (Nest, Biotech, China) at a density of 60% confluence. NPC cells were transfected with the mimics, inhibitor or plasmid using Lipofectamine TM 2000 (Invitrogen Biotechnology, China) according to the manufacturer's protocol. After 48 to 72 h, cells were collected for further experiments.

2.8. Cisplatin or cinobufotalin treatment in cells

cis-Diamminedichloroplatinum (cisplatin, DDP; Qilu Pharm Co. Ltd., Jinan, China) was resuspended in phosphate-buffered saline (PBS) (0.5 mg/ml). Drug sensitivity was determined by the 3-(4,5-dimethylthiazol-2-yl)-2,5-Diphenyltetrazolium bromide (MTT) assay. Cells were seeded in 96-well plates in 100 μ l RPMI-1640 medium supplemented with 10% FBS at 5 \times 10³ cells/well. Once attached, cells were treated with 2.5, 5, 10, 20 or 40 μ M Cisplatin or with 0.05, 0.1, 0.25, 0.5 0.75 or 1 μ M Cinobufotalin. For Cinobufotalin combined with DDP, cells were treated by Cinobufotalin and DDP with the same contraction at 0.05, 0.1, 0.25, 0.5 0.75 or 1 μ M and incubated at 37 $^{\circ}$ C in 5% CO₂ for 48 h. MTT cytotoxicity assays were then performed three times.

2.9. Nuclear and cytoplasmic extraction assay

Cell nuclear and cytoplasmic extraction assay was conducted using NE-PER[®] Nuclear and Cytoplasmic Extraction kit (Thermo Scientific Pierce, UK) according to the manufacturer's instructions. Briefly, cells were harvested and washed with PBS by pipetting, and were then incubated with ice-cold CER I for 10 min at 4 $^{\circ}$ C. After incubation, CER II extraction reagent was added to the reaction mixture for another 1 min and the lysate was centrifuged at 16000g for 5 min. The supernatant (cytoplasmic extract) was carefully transferred into a fresh microcentrifuge tube and stored in ice. The pellet was resuspended in NER extraction reagent and incubated for 40 min on ice. The suspension was then centrifuged at 16000g for 10 min, and the supernatant (nuclear extract) was transferred to a fresh microcentrifuge tube and stored on ice. The proteins were quantitated by BCA protein assay kit, and further analyzed by western blot analysis.

2.10. Western blot analysis

Cell lysates were separated by SDS-PAGE followed by blocking in 3% BSA (Bovine Serum Albumin), then incubated with primary antibodies against PI3K (1:1000), p-PI3K (Tyr⁴⁵⁸) (1:1000), AKT (1:1000), p-AKT (Ser⁴⁷³) (1:1000), MAP2K4(1:500), c-Jun (1:1000), MYH9 (1:1000), β -catenin (1:1000), GSK3 β (1:500), p-GSK3 β (1:1000), c-Myc (1:1000), E-cadherin (1:1000), N-cadherin (1:1000), Vimentin (1:1000), Nanog (1:1000), OCT-4 (1:1000), Sox2 (1:2000), TRAF6 (1:1000), ubiquitin (1:1000), β -actin (1:1000); and GAPDH (1:1000). The immunoreactive bands were visualized with chemiluminescence (ECL) (Millipore, Bedford, MA, USA), and images were captured with Minichemi imaging system (Sage, Beijing, China). All blot figures include the location of molecular weight/size markers.

2.11. Antibodies

The following antibodies used in this study for western blotting (WB), Immunohistochemistry (IHC) and immunofluorescence (IF) were: PI3K (4292S, Cell Signaling), p-PI3K (Tyr458) (11508-2, Singalway Antibody), AKT (4691, Cell Signaling), p-AKT (Ser473) (4060S, Cell Signaling), MAP2K4 (17340-1-AP, ProteinTech), c-Jun (9165S, Cell Signaling), MYH9 (60233-1-IG, ProteinTech), GSK3 β (22104-1-AP, ProteinTech), p-GSK3 β (5558S, Cell Signaling), c-Myc (AB32072, Abcam), E-cadherin (60335-1-IG, ProteinTech), N-cadherin (66219-1-IG, ProteinTech), β -catenin (51067-2-AP, ProteinTech), Vimentin (10366-1-AP, ProteinTech), Nanog (14295-1-AP,

ProteinTech), OCT-4 (60242-1-IG, ProteinTech), Sox2 (11064-1-AP, ProteinTech), TRAF6 (66498-1-IG, ProteinTech), ubiquitin (10201-2-AP, ProteinTech), β -actin (CW0264M), GAPDH (CW0100M) and Histone (#5748, Cell Signaling), CD133(#64326, Cell Signaling), CD44(#3570, Cell Signaling).

2.12. Transwell and Boyden chamber analysis

Transwell and boyden(BD Biosciences, NJ, USA) assay were performed to detect cell migration and invasion abilities. Cells were suspended in 100 μ l RPMI-1640 without serum and seeded into the top chamber of the transwells coated with Matrigel (BD Biosciences, NJ, USA) or left uncoated, and the bottom chambers were filled with 500 μ l RPMI-1640 supplemented with 10% FBS. After incubation, the filter was fixed, stained, and photographed. The number of stained cells that exhibited the ability to invade and migrate was counted. All experiments were performed three times.

2.13. In vivo metastasis assays in nude mice

All mice (BALB/C, nu/nu) were 4-weeks-old, female, weighing 11–13 g, approved by the BEIJING HFK BIOSCIENCE CO., LTD. For in vivo metastasis assays, 50 μ l of HONE1-EBV⁺ and 5-8F cells (5×10^6) overexpressing miR-BART22 or their control cells were injected under the liver capsule of each mouse ($N=8$ per group), and then carefully pushed its liver back into the abdominal cavity after cleaning and lightly pressing the pinhole with alcohol cotton balls for 1 min. The mice were maintained in a barrier facility on HEPA-filtered racks and fed an autoclaved laboratory rodent diet. All mice were euthanized after 6 weeks of study. Liver and colon tissues were subjected to fluorescent imaging using the LT-9MACIMSYSPLUS whole-body imaging system (Lighttools Research, Encinitas, CA, USA).

2.14. Establishing the subcutaneous xenograft mouse model

The subcutaneous xenograft mouse model was also established to determine the tumor formation abilities. A serial number of 1×10^6 , 5×10^5 , 1×10^5 , and 5×10^4 cells were injected into the mice ($N=6$ per group), and tumor-initiating frequencies were calculated using extreme limiting dilution analysis (<http://bioinf.wehi.edu.au/software/elda/>).

2.15. DDP-treatment survival experiment on nude mice

To establish an NPC mouse model, 6×10^5 miR-BART22-overexpressing HONE1 EBV⁺ or control cells, in 0.2 ml buffered saline, were intraperitoneally injected into the mice ($N=10$ per group). Tumors were allowed to grow for 3 days, and then the animals were divided into four groups for treatment testing: the miR-BART22+DDP group; the miR-BART22+ Normal saline (NS) group; the control cell + DDP (Mock) group and the miR-BART22+ NS group). Mice were intraperitoneally injected with NS or DDP(4 mg/kg) every 3 days respectively, and survival curves were analyzed using Kaplan-Meier analysis.

2.16. The cinobufotalin-treatment survival experiment on nude mice

5×10^6 miR-BART22 over-expressing in HONE1-EBV⁺ and 5-8F cells were intraperitoneally injected into the mice. The mice were subsequently randomized into 4 groups ($N=10$ per group). Ten days after injection, group 1 received the DDP (4 mg/kg), group 2 received cinobufotalin (4 mg/kg), group 3 received cinobufotalin with half dose (2 mg/kg), and group 4 received DDP combined with cinobufotalin (4 mg/kg, respectively) by intraperitoneal injection every 5 days. Finally, we observed the survival time of nude mice in different treatment group.

2.17. Immunohistochemistry (IHC)

Paraffin sections (4 μ m thickness) were prepared from in vivo experiments and used for immunohistochemistry to detect E-cadherin (1:200), N-cadherin (1:200), OCT4 (1:250), NANOG (1:100), MAP2K4 (1:100) protein expression. The indirect streptavidin-peroxidase method was used based on the manufacturer's instructions. Stained tissue sections were examined separately by two pathologists.

2.18. In situ hybridization (ISH)

In situ hybridization was conducted on paraffin-embedded specimens (4 μ m thickness). Paraffin sections were deparaffinized in xylene and rehydrated in graded alcohols and distilled water. After treating with proteinase K at 37 °C for 30 min, sections were rinsed, fixed, and then prehybridized for 2 h. Hybridization was performed with miR-BART22 Digoxigenin (DIG)-labeled probes designed and synthesized by BersinBio (Guangzhou, China). Slides were hybridized with DIF-labeled LNA probes overnight at 37 °C and were then washed and incubated with anti-DIG-HRP Fab fragments for 1 h at room temperature. Signals were visualized with the 3,3'-Diaminobenzidine (DAB) substrate (Maixin Biotech. Co., Ltd., Fuzhou, China).

2.19. Tumorsphere formation

After digestion, single cell suspensions were seeded into 6-well ultra-low-attachment plates (Corning, Inc., NY, USA) at a density of 5×10^3 cells/well and cultured in serum-free medium DMEM/F12 with FGF (20 ng/ml), EGF (20 ng/ml), and B27 (2%). After 2–3 weeks of incubation, tumor sizes were photographed using microscopy. Then single-cell suspensions were made to form new tumorspheres. The size and number of tumorspheres were analyzed after a continuous passage of three generations.

2.20. Side populations

For side population (SP) analysis, 1×10^6 cells (here we used HONE1 cells instead of HONE1-EBV⁺ with green fluorescence because of potential detection by the flow cytometer) were resuspended in DMEM containing 2% FBS, and treated with 5 μ g/ml The Hoechst 33342 stain (Sigma-Aldrich, MO, USA) was applied for 90 min at 37 °C with gentle blending every 10 min. Samples were simultaneously incubated with 50 μ mol/L of verapamil (Sigma-Aldrich, MO, USA), which served as negative controls. Cells were washed using ice-cold PBS and then subjected to flow cytometric analysis. Propidium iodide was used to identify dead cells.

2.21. Luciferase reporter assay

Luciferase reporter assay was used to examine the binding activation of miR-BART22 with PsiCHECK-2 vectors containing MAP2K4 wt 3'-UTR or mut 3'-UTR. The vector was co-transfected with miR-BART22 mimics, inhibitor or control sequences into cells, and luciferase activity was measured 48 h after transfection using the Dual-Luciferase Reporter Assay System (Promega Corporation, Madison, WI, USA). To examine the effect of c-Jun on transcription activity of MAP2K4, MYH9 and ubiquitin, fragments encoding c-Jun binding sites were cloned into pGL4.1-Basic luciferase reporter vector, and the c-Jun-binding site mutation vectors were constructed. These vectors and c-Jun plasmid were co-transfected into HONE1-EBV⁺ and 5-8F cells to detect the luciferase activity.

2.22. Ago2 immunoprecipitation (IP)

Cytoplasmic lysates were subjected to RNA immunoprecipitation (RIP) assays using an Ago2-specific antibody (Abcam, USA), and the EZ-Magna RIP™ RNA-Binding Protein Immunoprecipitation Kit (Millipore) according to the manufacturer's protocol.

2.23. Coimmunoprecipitation (Co-IP)

Co-IP was carried out using a Pierce Co-Immunoprecipitation kit (Thermo Scientific, USA) according to the manufacturer's instructions. Briefly, total proteins were extracted and quantified. A total of 1000 µg protein in 400 µL supernatant was incubated with 10 µg anti-Flag, anti-MYH9 or anti-IgG antibodies for 12 h at 4 °C. Beads were washed, eluted in sample buffer, and boiled for 10 min at 100 °C. Immune complexes were subjected to Coomassie brilliant blue staining, mass spectrometry, and western blot analysis. Anti-IgG was used as a negative control.

2.24. The chromatin immunoprecipitation (ChIP) assay

Chromatin immunoprecipitation assays were performed using a ChIP assay kit (Thermo Scientific, Waltham, MA, USA). According to the manufacturer's protocol, chromatin was crosslinked, isolated, and digested with Micrococcal Nuclease to obtain DNA fragments. The anti-c-Jun or IgG was added to the reaction systems for immunoprecipitation. After elution and purification, the recovered DNA fragments were subjected to qPCR and PCR. IgG served as a negative control.

2.25. Electrophoretic mobility shift assay (EMSA) analysis

The electrophoretic mobility shift assay was conducted using an EMSA Kit (BersinBio, Guangzhou, China) according to the manufacturer's instructions. Nuclear extracts were obtained from cells, and concentrations were determined using the BCA assay kit. EMSA was performed in a reaction mixture containing nuclear extracts and biotin-labeled probes. Competition or super-shift assays were performed by adding 100-fold excesses of cold competitors (unlabeled wild-type or mutant probes), or polyclonal rabbit anti-c-Jun (Cell Signaling Technology) to the reaction mixture. After electrophoresis and incubation, signals were recorded and analyzed.

2.26. Immunofluorescence and confocal microscopy

Cells were plated on coverslips in 48-well plates and cultured overnight to allow for cell adherence. After fixation with 4% paraformaldehyde and permeabilization with 0.2% Triton X-100, cells were incubated with antibodies. Cells were then counterstained with 0.2 mg/ml DAPI and visualized with a fluorescent confocal microscope (Carl Zeiss LSM800, Germany). GSK3β (1:50), β-catenin (1:100), MYH9 (1:50), CD44(1:100), CD133(1:100).

2.27. The cycloheximide (CHX) chase assay

Cells were transfected with scrambles or plasmids and were then incubated with 20 µmol/L MG132 for 0–12 h or left untreated. At different time points post 50 µg/ml CHX treatment, cells were harvested and prepared for Western blot analysis.

2.28. Statistical analysis

All the data were analyzed using SPSS 20.0 software (SPSS Inc. Chicago, IL, USA). The data are expressed as the means ± SD from at least three independent experiments. Statistical significance was determined using the Student's two-tailed *t*-test for

two groups, the one-way ANOVA for multiple groups, and the two-way ANOVA for tumor growth and the MTT assay. Correlation between gene expression and clinicopathological characters were analyzed using the Chi-square test. Log-rank tests were performed on Kaplan-Meier survival curves to elucidate any significant relationships between gene expression and overall survival in patients. Univariate and multivariate survival analysis was performed using the Cox proportional hazards regression model. All statistical tests were two-sided and *P* < .05 was considered statistically significant. * *P* < .05, ** *P* < .01 and *** *P* < .001.

3. Results

3.1. EBV-miR-BART22 promotes tumor stemness and DDP chemoresistance

Lentiviral vectors carrying miR-BART22 or control vectors were transfected into HONE1-EBV⁺ and 5-8F cell lines, respectively (Fig. S1a). MiR-BART22 levels were found to be increased in lentiviral-miR-BART22-transfected cells compared with control transfected cells using RT-qPCR (*P* < .05) (Fig. S1b). Subsequently, the sphere-forming assay revealed that miR-BART22 stimulated sphere growth (Fig. 1a). Next, the expression levels of CD133 and CD44 in miR-BART22-overexpressing cells were significantly higher than those in the control groups as measured using immunofluorescence (Fig. 1b). Moreover, flow cytometry analysis showed that side population ratio was markedly up-regulated in overexpressed miR-BART22 NPC cells (Fig. 1c). In the xenograft model, the estimated tumor-initiating frequency was 5×10^4 when the HONE1-EBV⁺-miR-BART22 cells were inoculated, while the tumor-initiating rate was 1×10^5 when the control cells were inoculated (Fig. 1d).

Lentiviral vectors carrying miR-BART22 or control vectors were transfected into HONE1-EBV⁺ and 5-8F cell lines, respectively (Fig. S1a). MiR-BART22 levels were found to be increased in lentiviral-miR-BART22-transfected cells compared with control transfected cells using RT-qPCR (*P* < .05) (Fig. S1b). Subsequently, the sphere-forming assay revealed that miR-BART22 stimulated sphere growth (Fig. 1a). Next, the expression levels of CD133 and CD44 in miR-BART22-overexpressing cells were significantly higher than those in the control groups as measured using immunofluorescence (Fig. 1b). Moreover, flow cytometry analysis showed that side population ratio was markedly up-regulated in overexpressed miR-BART22 NPC cells (Fig. 1c). In the xenograft model, the estimated tumor-initiating frequency was 5×10^4 when the HONE1-EBV⁺-miR-BART22 cells were inoculated, while the tumor-initiating rate was 1×10^5 when the control cells were inoculated (Fig. 1d).

For migration and invasion analysis, HONE1-EBV⁺-miR-BART22 and 5-8F-miR-BART22 cells or the respective controls were cultured in Transwell and Boyden chambers, respectively. As shown in Fig. 1e, miR-BART22 increased the cell migration and invasion abilities compared with those of the control groups. In vivo experiments, mice injected with HONE1-EBV⁺-BART22 or 5-8F-BART22 cells were all displayed extensively intrahepatic dissemination, while four of eight(4/8) mice in the HONE1-EBV⁺ control group and five of eight(5/8) mice in the 5-8F control group developed intrahepatic dissemination. Besides, six of eight(6/8) mice in HONE1-EBV⁺-BART22 group and seven of eight mice(7/8) in 5-8F-BART22 group exhibited intestinal metastasis. Only one mouse with intestinal metastasis was detected in their corresponding control groups (Fig. 1f). To study the influence of EBV-miR-BART22 on NPC chemotherapy efficacy, we first tested the viability of miR-BART22-overexpressing cells in different concentrations of DDP and inhibition rates were calculated 48 h after DDP treatment. Compared with the control cells, the IC50 of DPP increased from

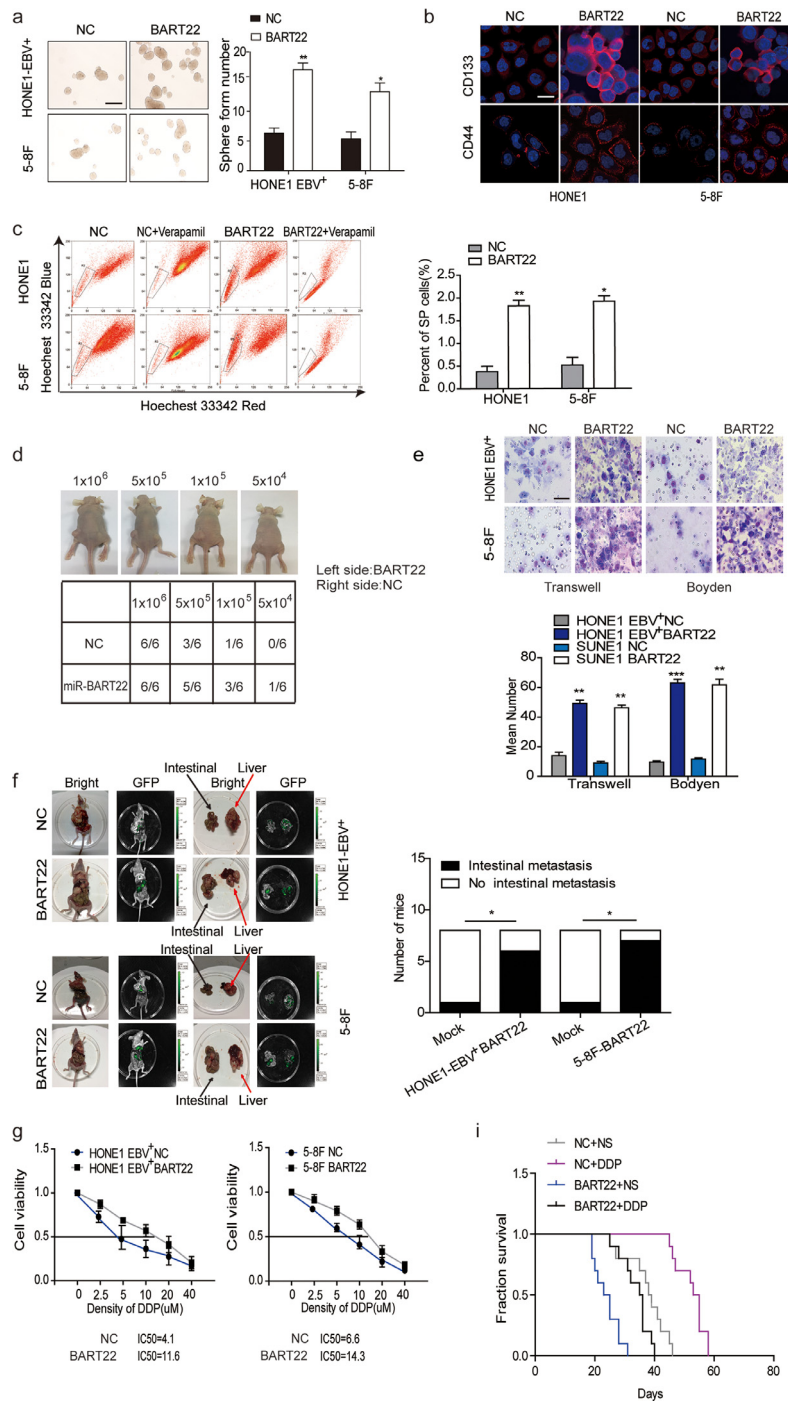


Fig. 1. EBV-miR-BART22 promotes tumor stemness and DDP chemoresistance (a) The sizes (left panel) and number of spheres (right panel) generated by the miR-BART22-overexpressing and their control NPC cells are shown; three independent experiments were performed. Original magnification, $\times 100$, scale bar, $200 \mu\text{m}$; (b) Immunofluorescence staining clearly shows higher CD44 and CD133 expression in the miR-BART22-expressing cells compared to their control cells, $\times 400$, scale bar, $25 \mu\text{m}$; (c) Percentages of SP cells are shown in the panel; three independent experiments were performed, $**P < .01$. HONE1 and 5-8F cells were transfected with BART22 mimics. Blank: HONE1 or 5-8F parental cells. (d) tumor formation in nude mice Injection of 10^6 , 5×10^5 , 10^4 or 5×10^4 cells with miR-BART22-overexpression or control cell, respectively in the left and right side ($n = 6$). (e) Effects on migration and invasion of miR-BART22 were measured by Transwell and Boyden Chamber assays in HONE1-EBV⁺-Lv-miR-BART22 and 5-8F-Lv-miR-BART22 cells. $\times 400$, scale bar, $50 \mu\text{m}$; $**P < .01$, $***P < .001$. (f) In vivo intrahepatic and intestinal metastasis assays results after HONE1-EBV⁺-Lv-miR-BART22 and 5-8F-Lv-miR-BART22 injection. Graph described the numbers of mice which occur metastasis or not; χ^2 test, $*P < .05$. (g) Dose-response curves of HONE1-EBV⁺ and 5-8F treated with miR-BART22 or miR-mock 48 h after treatment with DDP. Parametric generalized linear model with random effects. (h) Animals were divided into four groups: control group (NC) + Normal saline (NS), NC + DDP, BART22 + NS and BART22 + DDP (each group: $N = 10$). Xenograft tumors are shown for each group after 25 days of DDP or NS treatment. (i) Survival analysis was plotted. Log-rank test.

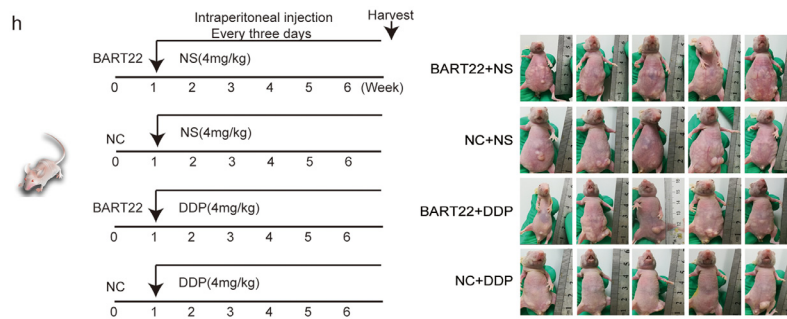


Fig. 1. Continued

4.1 to 11.6 μM in miR-BART22-overexpressing HONE1-EBV⁺ cells. Similarly, the IC₅₀ of DDP in miR-BART22-overexpressing 5-8F cells increased from 6.6 to 14.3 μM (Fig. 1g). Furthermore, we validated the chemotherapy resistance of miR-BART22-overexpressing cells in mice models. After miR-BART22-overexpressing or control cells were intraperitoneally injected into mice, mice were divided into four groups: [1] miR-BART22 + DDP, [2] miR-BART22 + Normal saline (NS), [3] normal control + DDP (NC + DDP), and [4] NS + NS cell groups (Fig. 1h). The growth of tumors was recorded in each group of mice. Kaplan-Meier analysis showed the survival times of mice in the NC + DDP and NC + NS groups were much longer than those in miR-BART22 + NS and miR-BART22 + DDP groups. Compared with the other three groups, BART22 + NS group showed the shortest survival time, and the NC + DDP group showed the longest survival time (Fig. 1i).

EBV-miR-BART22 inhibitors or controls were transfected into miR-BART22-overexpressing 5-8F and HONE1-EBV⁺ cells. RT-qPCR confirmed that the miR-BART22 inhibitor markedly inhibited miR-BART22 expression in both lines (Fig. S1c). The sphere-forming assay showed that the miR-BART22 inhibitor blocked the formation of tumor spheres (Fig. S1d). Using Transwell and Boyden Chambers, we observed that the miR-BART22 inhibitor reduced NPC cell migration and invasion (Fig. S1e). Subsequently, we examined the effect of the miR-BART22 inhibitor on DDP resistance. Result in Fig. S1f revealed that the IC₅₀ of DDP for the HONE1-EBV⁺ BART22 + IN-NC cells was 12.0 μM , while that of the control cells with miR-BART22 inhibitor was 4.9 μM . The IC₅₀ for DDP in HONE1-EBV⁺ cells was reduced from 5.4 to 3.2 μM after miR-BART22 Inhibitor transfection. Similarly, the IC₅₀ of DDP was 14.7 μM in miR-BART22-overexpressing 5-8F cells, while the miR-BART22-inhibited control cells were 5.8 μM (Fig. S1f). Taken together, the EBV-miR-BART22 inhibitor reversed the stimulation of miR-BART22 on NPC progression and chemoresistance.

EBV-miR-BART22 inhibitors or controls were transfected into miR-BART22-overexpressing 5-8F and HONE1-EBV⁺ cells. RT-qPCR confirmed that the miR-BART22 inhibitor markedly inhibited miR-BART22 expression in both lines (Fig. S1c). The sphere-forming assay showed that the miR-BART22 inhibitor blocked the formation of tumor spheres (Fig. S1d). Using Transwell and Boyden Chambers, we observed that the miR-BART22 inhibitor reduced NPC cell migration and invasion (Fig. S1e). Subsequently, we examined the effect of the miR-BART22 inhibitor on DDP resistance. Result in Fig. S1f revealed that the IC₅₀ of DDP for the HONE1-EBV⁺ BART22 + IN-NC cells was 12.0 μM , while that of the control cells with miR-BART22 inhibitor was 4.9 μM . The IC₅₀ for DDP in HONE1-EBV⁺ cells was reduced from 5.4 to 3.2 μM after miR-BART22 Inhibitor transfection. Similarly, the IC₅₀ of DDP was 14.7 μM in miR-BART22-overexpressing 5-8F cells, while the miR-BART22-inhibited control cells were 5.8 μM (Fig. S1f). Taken together, the EBV-miR-BART22 inhibitor reversed the stimulation of miR-BART22 on NPC progression and chemoresistance.

3.2. EBV-miR-BART22 activates the PI3K/AKT and GSK3 β / β -catenin signaling pathways

We assessed the influence of EBV-miR-BART22 on the PI3K/AKT and GSK3 β / β -catenin pathways. The data showed that overexpressed EBV-miR-BART22 induced phosphorylation of PI3K/AKT signaling. However, the expression change of total PI3K/AKT proteins was not observed. Further, total GSK3 β and phosphorylated GSK3 β proteins were found to be significantly downregulated, β -catenin protein expression was increased in EBV-miR-BART22-overexpressing NPC cells (Fig. 2a). In addition, tumor stemness and EMT pathways were also activated in EBV-miR-BART22-overexpressing NPC cells, which included the upregulated expression levels of *Nanog*, *OCT-4*, *SOX2*, *N-cadherin*, *Vimentin*, *c-Myc*, and the downregulated expression level of *E-cadherin*. Interestingly, the oncogenic transcription factor c-Jun was also induced by EBV-miR-BART22 in NPC cells. Finally, immunohistochemical staining indicated higher expression of *N-cadherin*, *Nanog* and *OCT4*, and lower expression of *E-cadherin* in liver-transplanted EBV-miR-BART22-overexpressing NPC tumor tissues compared with liver-transplanted control tumor tissues (Fig. 2b).

In a subsequent investigation, simultaneous introduction of the miR-BART22 or PI3K inhibitor LY294002 in miR-BART22-overexpressing NPC cells reversed the expression pattern mediated by miR-BART22 upregulation.

Moreover, the cycloheximide (CHX) chasing assay showed that miR-BART22 reduced the half-life of the GSK3 β protein. The effect of miR-BART22 on GSK3 β stability could be obviously alleviated by the proteasome inhibitor MG132 (Fig. 2c).

3.3. EBV-miR-BART22 directly targets MAP2K4

Bioinformatics analysis predicts MAP2K4 as a direct target of miR-BART22 (Fig. S2a). Western blot and RT-qPCR data demonstrated that miR-BART22 overexpression or miR-BART22 overexpression with the treatment of LY294002 resulted in downregulation or upregulation of MAP2K4 mRNA and protein levels (Fig. S2b–c). Moreover, immunohistochemistry of xenografts originating from miR-BART22-overexpressing NPC cells indicated a significant reduction in MAP2K4 protein expression, which was consistent with the in vitro findings (Fig. S2d). To verify if MAP2K4 is a direct target of miR-BART22, wild-type (Wt) or mutant (mt) 3'UTR psiCHECK vectors for MAP2K4 were co-transfected with miR-BART22 mimics or its inhibitors into HONE1-EBV⁺ cells. Luciferase reporter assays confirmed that miR-BART22 directly bound to the 3'UTR of MAP2K4 (Fig. S2e). To further validate this finding, we carried out RNA immunoprecipitation (IP). As shown in Fig. S2f, Ago2-bound miR-BART22 and MAP2K4 mRNA levels were markedly increased in HONE1-EBV⁺ cells. Further, MAP2K4 mRNA enrichment in the Ago2-IP was also increased by miR-BART22. These results indicated that MAP2K4 is a direct target of miR-BART22.

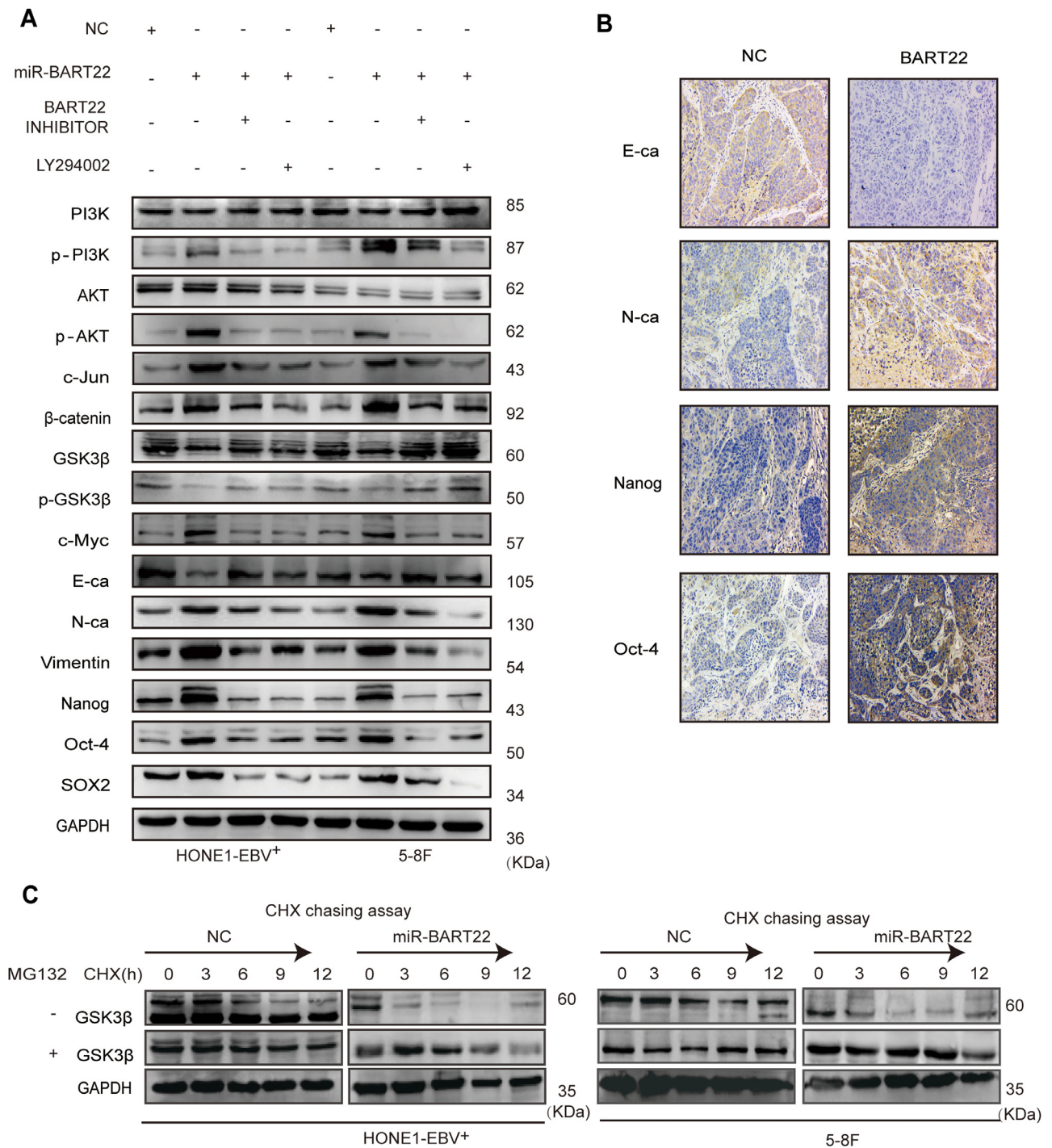


Fig. 2. EBV-miR-BART22 activates the PI3K/AKT/GSK3β/β-catenin signaling pathway (a) Protein levels of PI3K, p-PI3K, AKT, p-AKT, c-Jun, β-catenin, GSK3β, p-GSK3β, c-Myc, E-cadherin, N-cadherin, Vimentin, Nanog, OCT4 and Sox2 were measured by western blot after miR-BART22 overexpression. Levels of related proteins were reduced or increased after BART22 inhibitor transfection or LY294002 treatment. GAPDH served as controls. (b) Immunohistochemistry analysis of E-cadherin, N-cadherin, Nanog and OCT4 expression. Original magnification, ×200, scale bar, 100 μm. (c) Western blotting analysis of the effect of miR-BART22 overexpression on GSK3β stability in NPC cells treated with cycloheximide and MG132 at different time points, GAPDH served as controls.

Bioinformatics analysis predicts MAP2K4 as a direct target of miR-BART22 (Fig. S2a). Western blot and RT-qPCR data demonstrated that miR-BART22 overexpression or miR-BART22 overexpression with the treatment of LY294002 resulted in downregulation or upregulation of MAP2K4 mRNA and protein levels (Fig. S2b-c). Moreover, immunohistochemistry of xenografts originating from miR-BART22-overexpressing NPC cells indicated a significant reduction in MAP2K4 protein expression, which was consistent

with the in vitro findings (Fig. S2d). To verify if MAP2K4 is a direct target of miR-BART22, wild-type (Wt) or mutant (mt) 3'UTR psi-CHECK vectors for MAP2K4 were co-transfected with miR-BART22 mimics or its inhibitors into HONE1-EBV⁺ cells. Luciferase reporter assays confirmed that miR-BART22 directly bound to the 3'UTR of MAP2K4 (Fig. S2e). To further validate this finding, we carried out RNA immunoprecipitation (IP). As shown in Fig. S2f, Ago2-bound miR-BART22 and MAP2K4 mRNA levels were markedly increased

in HONE1-EBV⁺ cells. Further, MAP2K4 mRNA enrichment in the Ago2-IP was also increased by miR-BART22. These results indicated that MAP2K4 is a direct target of miR-BART22.

3.4. MAP2K4 reduces MYH9 expression by downregulating PI3K/AKT/c-Jun-mediated stimulation

Coimmunoprecipitation (Co-IP) combined with mass spectrometry were used in HONE1-EBV⁺ cells to screen for potential interacting proteins of MAP2K4. MYH9 protein was screened as a potential interacting MAP2K4 protein. Although exogenous Co-IP did not indicate the combination between MAP2K4 and MYH9 (Fig. S3a), we accidentally found that MYH9 mRNA and protein levels were reduced in MAP2K4-overexpressing NPC cells compared with that of the control cells (Fig. S3b–c). Based on the ChIP-seq binding peaks in conjunction with UCSC, PROMO and JASPAR bioinformatics software, three c-Jun binding motifs at +22,898 to +22,906 (Site A), –7991 to –7979 (Site B), and –9578 to –9566 (Site C) were found within the transcription regulatory region of MYH9 (Fig. 3a). Knocking down c-Jun significantly reduced MYH9 mRNA and protein levels by using qPCR and Western blot assays, respectively (Fig. 3b–c). Further, the chromatin immunoprecipitation (ChIP) and the electrophoretic mobility shift assay (EMSA) verified that c-Jun bound to all the predicted sites inside the MYH9 transcriptional regulation region in HONE1-EBV⁺ and 5-8F cells (Fig. 3d–e). The luciferase reporter assays confirmed markedly upregulated luciferase activity in NPC cells after c-Jun cDNA transfection compared with that of the control cells (Fig. 3f). MAP2K4 was found to suppress PI3K/AKT/c-Jun signaling, which caused decreased the combination of c-Jun with MYH9 promoter (Fig. 3h) and thus suppressed MYH9 mRNA and protein levels (Fig. 3g–i).

Coimmunoprecipitation (Co-IP) combined with mass spectrometry were used in HONE1-EBV⁺ cells to screen for potential interacting proteins of MAP2K4. MYH9 protein was screened as a potential interacting MAP2K4 protein. Although exogenous Co-IP did not indicate the combination between MAP2K4 and MYH9 (Fig. S3a), we accidentally found that MYH9 mRNA and protein levels were reduced in MAP2K4-overexpressing NPC cells compared with that of the control cells (Fig. S3b–c). Based on the ChIP-seq binding peaks in conjunction with UCSC, PROMO and JASPAR bioinformatics software, three c-Jun binding motifs at +22,898 to +22,906 (Site A), –7991 to –7979 (Site B), and –9578 to –9566 (Site C) were found within the transcription regulatory region of MYH9 (Fig. 3a). Knocking down c-Jun significantly reduced MYH9 mRNA and protein levels by using qPCR and Western blot assays, respectively (Fig. 3b–c). Further, the chromatin immunoprecipitation (ChIP) and the electrophoretic mobility shift assay (EMSA) verified that c-Jun bound to all the predicted sites inside the MYH9 transcriptional regulation region in HONE1-EBV⁺ and 5-8F cells (Fig. 3d–e). The luciferase reporter assays confirmed markedly upregulated luciferase activity in NPC cells after c-Jun cDNA transfection compared with that of the control cells (Fig. 3f). MAP2K4 was found to suppress PI3K/AKT/c-Jun signaling, which caused decreased the combination of c-Jun with MYH9 promoter (Fig. 3h) and thus suppressed MYH9 mRNA and protein levels (Fig. 3g–i).

3.5. MYH9 interacts with GSK3 β and promotes GSK3 β protein ubiquitin degradation

The DOMINE database is used to predict that MYH9 protein interacts with GSK3 β . Subsequently, Co-IP analysis and immunofluorescence indicated that MYH9 bound GSK3 β and co-localized in the cytoplasm (Fig. 4a). Further, we observed that MYH9 downregulated GSK3 β and phosphorylated GSK3 β protein levels and upregulated β -catenin protein level. However, elevated MYH9 did not change GSK3 β mRNA expression (Fig. S4a–b). Subsequently, we

employed the cycloheximide (CHX) chasing assay (Fig. 4b) to examine the effects of MYH9 on GSK3 β protein stability. Co-IP assays indicated that MYH9 overexpression promoted GSK3 β and ubiquitin separation and facilitated the separation of GSK3 β from the ubiquitin ligation complex composed of TRAF6 in HONE1-EBV⁺ cells (Fig. 4c). GSK3 β K183 was identified as the ubiquitination site [35]. Plasmids with the GSK3 β 183R mutant and wild-type GSK3 β were transfected into MYH9-overexpressed HONE1-EBV⁺, and Co-IP assay showed that GSK3 β K183R mutant induced the separation of GSK3 β and ubiquitin and prevented the interaction of GSK3 β and ubiquitin ligation complex composed of TRAF6 (Fig. 4d). Finally, we detected the increased nuclear translocation of β -catenin in MYH9-overexpressing NPC cells (Fig. 4e). By nuclear and cytoplasmic extraction assay, we confirmed that MYH9 up-regulation induced the nuclear enrichment of β -catenin, whereas silencing MYH9 impaired the nuclear enrichment of β -catenin in NPC cells (Fig. 4f).

The DOMINE database is used to predict that MYH9 protein interacts with GSK3 β . Subsequently, Co-IP analysis and immunofluorescence indicated that MYH9 bound GSK3 β and co-localized in the cytoplasm (Fig. 4a). Further, we observed that MYH9 downregulated GSK3 β and phosphorylated GSK3 β protein levels and upregulated β -catenin protein level. However, elevated MYH9 did not change GSK3 β mRNA expression (Fig. S4a–b). Subsequently, we employed the cycloheximide (CHX) chasing assay (Fig. 4b) to examine the effects of MYH9 on GSK3 β protein stability. Co-IP assays indicated that MYH9 overexpression promoted GSK3 β and ubiquitin separation and facilitated the separation of GSK3 β from the ubiquitin ligation complex composed of TRAF6 in HONE1-EBV⁺ cells (Fig. 4c). GSK3 β K183 was identified as the ubiquitination site [35]. Plasmids with the GSK3 β 183R mutant and wild-type GSK3 β were transfected into MYH9-overexpressed HONE1-EBV⁺, and Co-IP assay showed that GSK3 β K183R mutant induced the separation of GSK3 β and ubiquitin and prevented the interaction of GSK3 β and ubiquitin ligation complex composed of TRAF6 (Fig. 4d). Finally, we detected the increased nuclear translocation of β -catenin in MYH9-overexpressing NPC cells (Fig. 4e). By nuclear and cytoplasmic extraction assay, we confirmed that MYH9 up-regulation induced the nuclear enrichment of β -catenin, whereas silencing MYH9 impaired the nuclear enrichment of β -catenin in NPC cells (Fig. 4f).

Interestingly, we unexpectedly observed that MYH9 upregulated ubiquitin mRNA and protein expressions through stimulating PI3K/AKT/c-Jun pathway. Firstly we found that ubiquitin mRNA levels were induced in MYH9-overexpressing NPC cells compared with the control cells (Fig. S4c). UCSC, PROMO, and JASPAR bioinformatic softwares predicted c-Jun as the potential transcription factor of ubiquitin (Fig. S4d), c-Jun overexpression significantly enhanced ubiquitin mRNA expression and protein levels (Fig. S4e–f). The ChIP, EMSA and luciferase reporter assays showed the protein-DNA interactions between c-Jun and all the predicted sites of the ubiquitin promoter in HONE1-EBV⁺ and 5-8F cells (Fig. 5a–c). Suppressing pPI3K using LY294002 in MYH9-overexpressing NPC cells significantly reduced PI3K/AKT/c-Jun (Fig. 5d) and further decreased the binding of c-Jun with the ubiquitin promoter (Fig. 5e–f) and downregulating ubiquitin mRNA and protein levels (Fig. 5g,d). Finally, we observed that ubiquitin overexpression achieved by transfecting ubiquitin cDNA increased the level of GSK3 β ubiquitination (Fig. S4g) and thus reduced GSK3 β protein expression and upregulated TRAF6 expression in NPC cells with MYH9 silenced (Fig. S4h). Collectively, MYH9 interacts with GSK3 β and promotes GSK3 β protein ubiquitination degradation by activating PI3K/AKT/c-Jun-induced ubiquitin expression, which thus increases β -catenin expression and its nuclear translocation.

Interestingly, we unexpectedly observed that MYH9 upregulated ubiquitin mRNA and protein expressions through stimulating PI3K/AKT/c-Jun pathway. Firstly we found that ubiquitin mRNA levels were induced in MYH9-overexpressing NPC cells compared

with the control cells (Fig. S4c). UCSC, PROMO, and JASPAR bioinformatic softwares predicted c-Jun as the potential transcription factor of *ubiquitin* (Fig. S4d), c-Jun overexpression significantly enhanced *ubiquitin* mRNA expression and protein levels (Fig. S4e–f). The ChIP, EMSA and luciferase reporter assays showed the protein-DNA interactions between c-Jun and all the predicted sites of the *ubiquitin* promoter in HONE1-EBV⁺ and 5-8F cells (Fig. 5a–c). Suppressing pPI3K using LY294002 in *MYH9*-overexpressing NPC cells significantly reduced *PI3K/AKT/c-Jun* (Fig. 5d) and further decreased the binding of c-Jun with the *ubiquitin* promoter (Fig. 5e–f) and downregulating *ubiquitin* mRNA and protein levels (Fig. 5g,d). Finally, we observed that *ubiquitin* overexpression achieved by transfecting *ubiquitin* cDNA increased the level of *GSK3β* ubiquitination (Fig. S4g) and thus reduced *GSK3β* protein expression and upregulated TRAF6 expression in NPC cells with *MYH9* silenced (Fig. S4h). Collectively, *MYH9* interacts with *GSK3β* and promotes *GSK3β* protein ubiquitination degradation by activating *PI3K/AKT/c-Jun*-induced *ubiquitin* expression, which thus increases β -catenin expression and its nuclear translocation.

3.6. MAP2K4 antagonizes the action of EBV-miR-BART22

MAP2K4 plasmids or empty plasmids were respectively transfected into miR-BART22-overexpressing NPC cells and increased *MAP2K4* mRNA and protein expression levels were observed in miR-BART22-overexpressing NPC cells (Supplementary Fig. S5a–b). Overexpressed *MAP2K4* blocked tumor stemness, cell migration and invasion by the tumorsphere formation (Fig. S5c), Transwell and Boyden Chamber (Fig. S5d) assays. The DDP chemoresistance assay revealed significant downregulation of IC50 value in *MAP2K4*-overexpressing cells compared with that of the control cells (Fig. S5e).

MAP2K4 plasmids or empty plasmids were respectively transfected into miR-BART22-overexpressing NPC cells and increased *MAP2K4* mRNA and protein expression levels were observed in miR-BART22-overexpressing NPC cells (Supplementary Fig. S5a–b). Overexpressed *MAP2K4* blocked tumor stemness, cell migration and invasion by the tumorsphere formation (Fig. S5c), Transwell and Boyden Chamber (Fig. S5d) assays. The DDP chemoresistance assay revealed significant downregulation of IC50 value in *MAP2K4*-overexpressing cells compared with that of the control cells (Fig. S5e).

Western blot analysis showed that cells with *MAP2K4* plasmids treatment inhibited *pPI3K*, *pAKT*, *c-Jun*, *MYH9*, β -catenin, *OCT4*, *NANOG*, *SOX2*, *Vimentin*, *N-cadherin*, and *c-Myc* expressions but increased the *E-cadherin*, *GSK3β*, and *p-GSK3β* expressions (Fig. S5f).

Western blot analysis showed that cells with *MAP2K4* plasmids treatment inhibited *pPI3K*, *pAKT*, *c-Jun*, *MYH9*, β -catenin, *OCT4*, *NANOG*, *SOX2*, *Vimentin*, *N-cadherin*, and *c-Myc* expressions but increased the *E-cadherin*, *GSK3β*, and *p-GSK3β* expressions (Fig. S5f).

Further, we found the reduced *GSK3β* ubiquitination level in miR-BART22-overexpressing HONE1-EBV⁺ cells transfected with *MAP2K4* (Fig. S5g). Moreover, transiently transfecting *MAP2K4* into miR-BART22-overexpressing NPC cells reduced the binding of c-Jun with *MYH9* or the *ubiquitin* promoter using the ChIP assays (Fig. S5h–i). We also detected the decreased *ubiquitin* and *MYH9* mRNA levels after *MAP2K4* transfection in miR-BART22-overexpressed NPC cells (Fig. S5j–k).

Further, we found the reduced *GSK3β* ubiquitination level in miR-BART22-overexpressing HONE1-EBV⁺ cells transfected with *MAP2K4* (Fig. S5g). Moreover, transiently transfecting *MAP2K4* into miR-BART22-overexpressing NPC cells reduced the binding of c-Jun with *MYH9* or the *ubiquitin* promoter using the ChIP assays (Fig. S5h–i). We also detected the decreased *ubiquitin* and *MYH9* mRNA levels after *MAP2K4* transfection in miR-BART22-overexpressed NPC cells (Fig. S5j–k).

3.7. Knocking down MYH9 antagonizes the action of EBV-miR-BART22

siRNAs-*MYH9* were transfected into miR-BART22-overexpressing NPC cells, and qPCR and Western blot analysis showed reduced *MYH9* mRNA and protein expressions (Fig. S6a–b). As expected, the percentage of SP cells was obviously reduced after interference with *MYH9* in the miR-BART22-overexpressing NPC cells (Fig. S6c). Assays using transwell and Boyden Chamber showed that *MYH9* knockdown reversed miR-BART22-induced cell migration and invasion (Fig. S6d). Western blot analysis also showed that siRNAs-*MYH9* treatment of NPC cells decreased *pPI3K*, *pAKT*, *c-Jun*, β -catenin, *OCT4*, *NANOG*, *SOX2*, *Vimentin*, *N-cadherin*, and *c-Myc* expression but increased the *E-cadherin*, *GSK3β* and *p-GSK3β* levels (Fig. S6e). In addition, *GSK3β* ubiquitination level was also reduced (Fig. S6f). Further, silencing *MYH9* also reduced the binding of c-Jun with the *ubiquitin* promoter using the ChIP assay (Fig. S6g–h) in miR-BART22-overexpressing NPC cells. Finally, reduced *ubiquitin* mRNA and protein levels were also found in miR-BART22-overexpressing NPC cells with *MYH9* knockdown (Fig. S6i–j).

siRNAs-*MYH9* were transfected into miR-BART22-overexpressing NPC cells, and qPCR and Western blot analysis showed reduced *MYH9* mRNA and protein expressions (Fig. S6a–b). As expected, the percentage of SP cells was obviously reduced after interference with *MYH9* in the miR-BART22-overexpressing NPC cells (Fig. S6c). Assays using transwell and Boyden Chamber showed that *MYH9* knockdown reversed miR-BART22-induced cell migration and invasion (Fig. S6d). Western blot analysis also showed that siRNAs-*MYH9* treatment of NPC cells decreased *pPI3K*, *pAKT*, *c-Jun*, β -catenin, *OCT4*, *NANOG*, *SOX2*, *Vimentin*, *N-cadherin*, and *c-Myc* expression but increased the *E-cadherin*, *GSK3β* and *p-GSK3β* levels (Fig. S6e). In addition, *GSK3β* ubiquitination level was also reduced (Fig. S6f). Further, silencing *MYH9* also reduced the binding of c-Jun with the *ubiquitin* promoter using the ChIP assay (Fig. S6g–h) in miR-BART22-overexpressing NPC cells. Finally, reduced *ubiquitin* mRNA and protein levels were also found in miR-BART22-overexpressing NPC cells with *MYH9* knockdown (Fig. S6i–j).

3.8. Cinobufotalin reversed EBV-miR-BART22-induced DDP resistance

To study the influence of cinobufotalin on EBV-miR-BART22 on NPC DDP chemotherapy efficacy, we firstly tested the viability of miR-BART22-overexpressing cells in using cinobufotalin combined with DDP. We observed that cinobufotalin markedly reduced the IC50 value in miR-BART22-overexpressing NPC cells. Compared with the DDP group, the IC50 value of DDP in miR-BART22-overexpressing NPC cells was significantly reduced when combined with cinobufotalin (Fig. 6a–b). Next, we observed that the survival time of nude mice with DDP treatment was a little shorter than those using half-dose cinobufotalin and significantly lower than those with the treatment of the same dose cinobufotalin. More interestingly, nude mice with the combined usage of the same DDP and cinobufotalin dose showed the longest survival time compared to other three groups. The average survival times of nude mice injected with HONE1-EBV⁺-BART22 cells in the cinobufotalin, DDP, half-dose cinobufotalin, and DDP+cinobufotalin groups were 35.8, 28.6, 31.7, 43 days, respectively. The average survival times of the nude mice injected with 5-8F-BART22 cells in the cinobufotalin, DDP, half-dose cinobufotalin, and DDP+cinobufotalin groups were 36.4, 32, 33.2, and 44.3 days, respectively (Fig. 6c–d). In addition, the weights of the mice in each group were measured, and the changes in weight are shown in Fig. S7a–b. We found that the weight of the mice in the DDP and cinobufotalin half-dose group was markedly reduced compared with those in the

DDP+cinobufotalin and cinobufotalin groups. The growth status of mice was observed at different times. Compared with the other three groups, cinobufotalin combined with the DDP group had better growth status and smaller tumor burden(Fig. S7c).

To study the influence of cinobufotalin on EBV-miR-BART22 on NPC DDP chemotherapy efficacy, we firstly tested the viability of miR-BART22-overexpressing cells in using cinobufotalin combined with DDP. We observed that cinobufotalin markedly reduced the IC50 value in miR-BART22-overexpressing NPC cells. Compared with the DDP group, the IC50 value of DDP in miR-BART22-overexpressing NPC cells was significantly reduced when combined with cinobufotalin. (Fig. 6a–b). Next, we observed that the survival time of nude mice with DDP treatment was a little shorter than those using half-dose cinobufotalin and significantly lower than those with the treatment of the same dose cinobufotalin. More interestingly, nude mice with the combined usage of the same DDP and cinobufotalin dose showed the longest survival time compared to other three groups. The average survival times of nude mice injected with HONE1-EBV⁺-BART22 cells in the cinobufotalin, DDP, half-dose cinobufotalin, and DDP+cinobufotalin groups were 35.8, 28.6, 31.7, 43 days, respectively. The average survival times of the nude mice injected with 5-8F-BART22 cells in the cinobufotalin, DDP, half-dose cinobufotalin, and DDP+cinobufotalin groups were 36.4, 32, 33.2, and 44.3 days, respectively(Fig. 6c–d). In addition, the weights of the mice in each group were measured, and the changes in weight are shown in Fig. S7a–b. We found that the weight of the mice in the DDP and cinobufotalin half-dose group was markedly reduced compared with those in the DDP+cinobufotalin and cinobufotalin groups. The growth status of mice was observed at different times. Compared with the other three groups, cinobufotalin combined with the DDP group had better growth status and smaller tumor burden (Fig. S7c).

3.9. Cinobufotalin inhibited EMT and tumor stemness signals by inducing MAP2K4 in miR-BART22-overexpressing nasopharyngeal carcinoma

Using transwell, Boyden, and sphere-forming assays, we showed that cinobufotalin markedly blocked cell invasion, migration, and the formation of tumorspheres induced by miR-BART22 in NPC cells(Fig. S7d–f). Bioinformatics analysis predicted +902~+908 of MAP2K4 promoter as the binding site of c-Jun (Fig. S7g). In subsequent study, qPCR identified that c-Jun overexpression markedly decreased MAP2K4 mRNA expression (Fig. 6e). Next, the ChIP and luciferase reporter assays showed the protein-DNA interactions between c-Jun and the predicted site of the MAP2K4 promoter in NPC cells(Fig. 6f–g). Using pPI3K inhibitor LY294002 in NPC cells, the expression level of pPI3K/pAKT/c-Jun was markedly reduced (Fig. S7h), which decreased the binding of c-Jun with MAP2K4 promoter(Fig. S7i) and thus increased the expression of MAP2K4 mRNA and protein levels(Fig. S7j,h). These data demonstrated that pPI3K/pAKT/c-Jun negatively modulated MAP2K4 expression in NPC. In the subsequent investigation, we observed that MAP2K4 mRNA and protein levels(Fig. 6h,j) were obviously induced by cinobufotalin via reducing pPI3K/pAKT/c-Jun-mediated transcription suppression of MAP2K4 promoter(Fig. 6I). Furthermore, MYH9/GSK3 β / β -catenin signal and its downstream tumor stemness and EMT signalings were observed to be significantly attenuated, which included the reduced expression levels of N-cadherin, Vimentin, NANOG, OCT4, SOX2, β -catenin, c-Myc protein levels and elevated E-cadherin, GSK3 β , and p-GSK3 β protein levels in miR-BART22-overexpressing NPC cells treated with cinobufotalin(Fig. 6j).

Using transwell, Boyden, and sphere-forming assays, we showed that cinobufotalin markedly blocked cell invasion, migration, and

the formation of tumorspheres induced by miR-BART22 in NPC cells(Fig. S7d–f). Bioinformatics analysis predicted +902~+908 of MAP2K4 promoter as the binding site of c-Jun (Fig. S7g). In subsequent study, qPCR identified that c-Jun overexpression markedly decreased MAP2K4 mRNA expression (Fig. 6e). Next, the ChIP and luciferase reporter assays showed the protein-DNA interactions between c-Jun and the predicted site of the MAP2K4 promoter in NPC cells(Fig. 6f–g). Using pPI3K inhibitor LY294002 in NPC cells, the expression level of pPI3K/pAKT/c-Jun was markedly reduced (Fig. S7h), which decreased the binding of c-Jun with MAP2K4 promoter(Fig. S7i) and thus increased the expression of MAP2K4 mRNA and protein levels(Fig. S7j,h). These data demonstrated that pPI3K/pAKT/c-Jun negatively modulated MAP2K4 expression in NPC. In the subsequent investigation, we observed that MAP2K4 mRNA and protein levels(Fig. 6h,j) were obviously induced by cinobufotalin via reducing pPI3K/pAKT/c-Jun-mediated transcription suppression of MAP2K4 promoter(Fig. 6I). Furthermore, MYH9/GSK3 β / β -catenin signal and its downstream tumor stemness and EMT signalings were observed to be significantly attenuated, which included the reduced expression levels of N-cadherin, Vimentin, NANOG, OCT4, SOX2, β -catenin, c-Myc protein levels and elevated E-cadherin, GSK3 β , and p-GSK3 β protein levels in miR-BART22-overexpressing NPC cells treated with cinobufotalin(Fig. 6j).

3.10. Increased EBV-miR-BART22 and reduced MAP2K4 expressions in NPC

EBV-miR-BART22 expression was markedly upregulated in NPC tissues compared with NP tissues by qPCR analysis (Fig. 7a, $p < .001$). As show in Fig. 7b, MAP2K4 mRNA expression was significantly lower in NPC than in NP samples($p < .001$). Further, we found that miR-BART22 expression was negatively correlated with MAP2K4 mRNA expression in NPC tissues (Fig. 7c, $\gamma = -0.2820, p = .0277$). In line with mRNA data, the increased miR-BART22 expression was showed in NPC tissues compared to NP tissues (Fig. 7d). Inversely, upregulated MAP2K4 protein was observed in NP tissues compared to NPC tissues (Fig. 7e). The clinical characteristics associated with miR-BART22 or MAP2K4 are summarized in Table S1–2. Increased miR-BART22 expression was positively correlated with clinical stage($p = .006$) (I-II vs. III-IV), tumor size (T classification; $p = .032$), lymph node metastasis (N classification; $p = .008$) (N0-N1 vs. N2–3). Reduced MAP2K4 expression was negatively correlated with clinical stage($p = .015$) (I-II vs. III-IV), tumor size (T classification; $p = .035$). Moreover, increased miR-BART22 expression had poorer overall survival rates by Kaplan-Meier survival analysis (Fig. 7f) ($p = .003$). Inversely, increased MAP2K4 expression had better overall survival rates by Kaplan-Meier survival analysis (Fig. 7g) ($p < .001$). NPC patients with low MAP2K4 expression and high expression of miR-BART22 had the worst survival prognosis compared to other 3 groups in Fig. 7h ($p < .001$). We did not find a significant association between miR-BART22 expression and clinical stage in stratified analysis of survival analysis. However, we observed that increased MAP2K4 expression showed the better survival prognosis compared to patients with reduced MAP2K4 expression in III-V stage (Fig. 7i–j) ($p = .003$).

4. Discussion

In this study, we firstly demonstrated that EBV-miR-BART22 acts as an oncogene that promotes tumor stemness, metastasis and DDP chemotherapy resistance using in vitro and in vivo assays. It is well established that the activation of PI3K/AKT and GSK3 β / β -catenin [36,37] and their downstream tumor stemness and EMT signals is key factor in promoting tumor stemness [38], metastasis

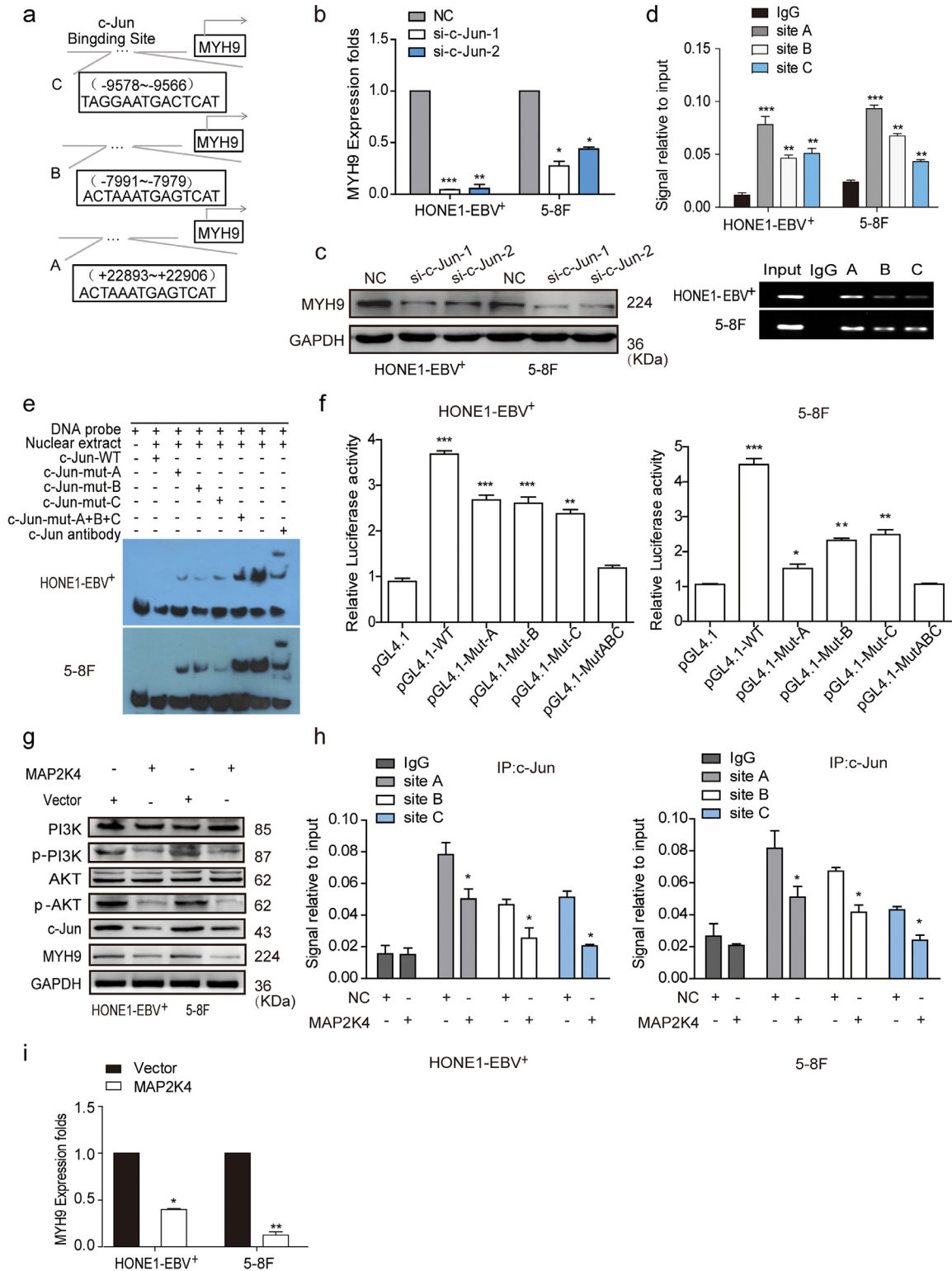


Fig. 3. MAP2K4 reduces MYH9 by downregulating PI3K/AKT/c-Jun-mediated stimulation. (a) Bioinformatics analysis was used to predict the binding sites of c-Jun within promoter of MYH9. (b)(c) QPCR (n = 3 independent experiments, Student's t-test) and Western blot analysis of MYH9 expression in c-Jun-silenced NPC cells and their control cells. (d) Chromatin immunoprecipitation analysis (comparison of all groups vs. IgG group) (n = 3 independent experiments, one-way ANOVA) of c-Jun binding to the MYH9 promoter. (e) The protein-DNA interactions between c-Jun and MYH9 promoter were determined using the electrophoretic mobility shift assay. (f) Luciferase reporter assays (comparison of all groups vs. control group) (n = 3 independent experiments, one-way ANOVA) were performed to confirm c-Jun binding to the MAP2K4 promoter. (g) Protein levels of PI3K, p-PI3K, AKT, p-AKT, c-Jun and MYH9 were measured by western blot in NPC cells treated with MAP2K4 plasmids. (h) Chromatin immunoprecipitation analysis of c-Jun binding to MYH9 promoter in MAP2K4-overexpressed HONE1-EBV⁺ and 5-8F cells. All data are presented as the means ± SD. Experiments were repeated three times. *P < .05. (i) QPCR analysis of MYH9 expression in MAP2K4-transfected HONE1-EBV⁺ and 5-8F cells and their control cells (n = 3 independent experiments, Student's t-test). *P < .05, **P < .01.

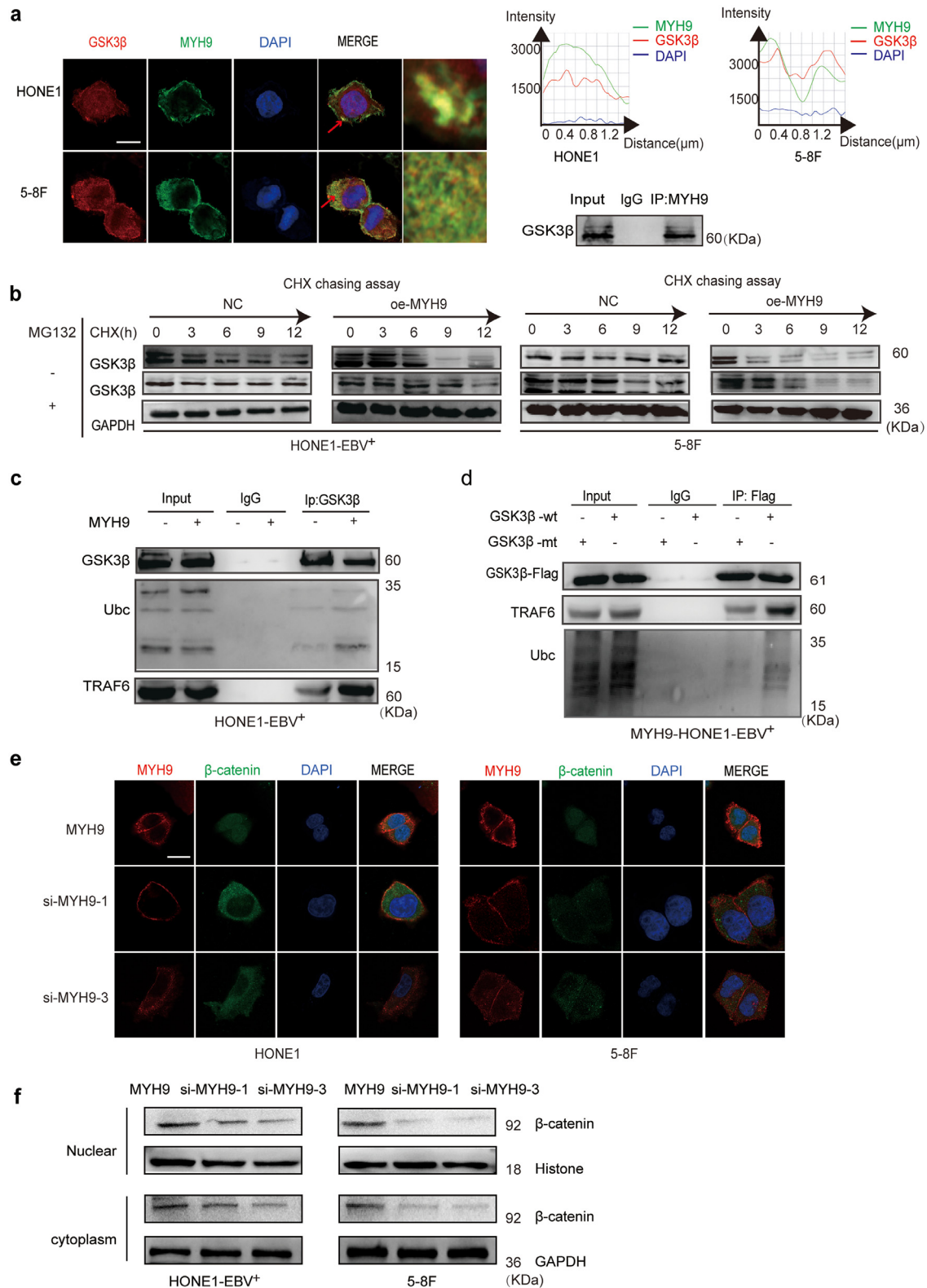


Fig. 4. MYH9 interacts with GSK3 β to promote GSK3 β ubiquitin protein degradation. (a) Immunofluorescence co-staining of GSK3 β and MYH9 to detect colocalization. The fluorescence intensities along the red arrow crossing the cytoplasm were calculated to show the colocalisation of GSK3 β and MYH9, scale bar, 25 μ m; Co-immunoprecipitation analysis of the effect of MYH9 on the interaction with GSK3 β in HONE1-EBV⁺ cells. (b) Western blotting analysis of the effect of MYH9 overexpression on GSK3 β stability in NPC cells treated with cycloheximide and MG132 at different time points, GAPDH served as controls. (c) Co-immunoprecipitation analysis of the effect of MYH9 on the interaction between GSK3 β , ubiquitin and TRAF6 in HONE1-EBV⁺ cells. (d) Co-immunoprecipitation analysis of ubiquitin, TRAF6 and wild GSK3 β or mutant GSK3 β in MYH9-overexpressed HONE1-EBV⁺ cells. (e) Immunofluorescence co-staining of MYH9 and GSK3 β expression and localization in MYH9-overexpressed or MYH9-depleted HONE1-EBV⁺ and 5-8F cells. Scale bar, 25 μ m. (f) Nuclear and cytoplasmic proteins were extracted for β -catenin detection by western blotting. (For interpretation of the references to colour in this figure legend, the reader is referred to the web version of this article.)

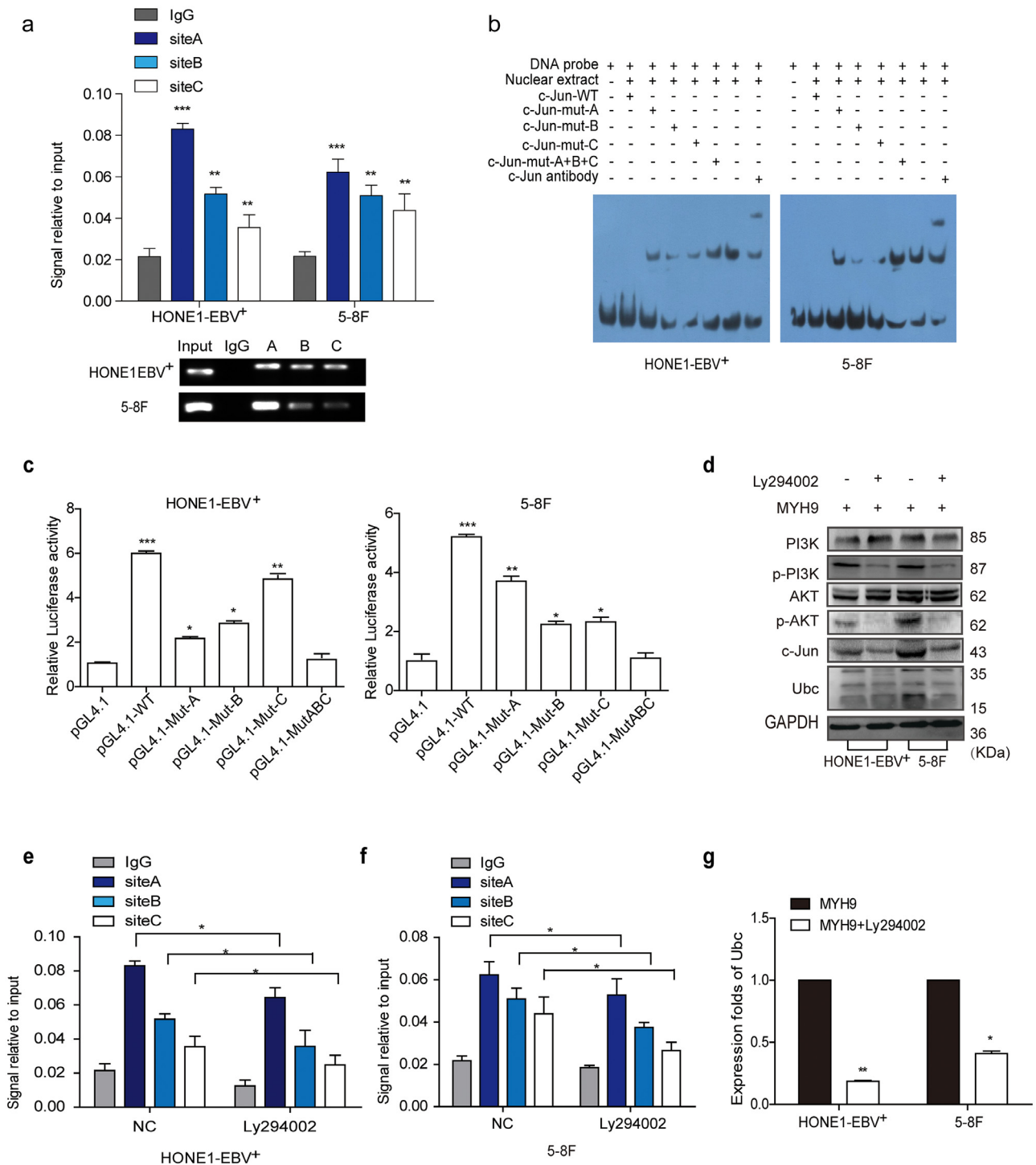


Fig. 5. MYH9 promotes ubiquitin transcription via PI3K/AKT/c-Jun.

(a) Chromatin immunoprecipitation analysis (comparison of all groups vs. IgG group) (n = 3 independent experiments, one-way ANOVA) of c-Jun binding to the Ubc promoter. (b) The protein-DNA interactions between c-Jun and Ubc promoter were determined using the electrophoretic mobility shift assay. (c) Luciferase reporter assays (comparison of all groups vs. control group) (n = 3 independent experiments, one-way ANOVA) were performed to confirm c-Jun binding to the Ubc promoter.

(d) Protein levels of PI3K, p-PI3K, AKT, p-AKT, c-Jun and Ubc were measured by western blot in NPC cells treated with MYH9 plasmids or both treated with LY294002. (e-f) Chromatin immunoprecipitation analysis of c-Jun binding to Ubc promoter in HONE1-EBV⁺ and 5-8F cells treated with LY294002. (g) QPCR analysis of Ubc mRNA levels in MYH9 over-expressed NPC cells with LY294002 transfected (n = 3 independent experiments, Student's t-test). All data are presented as the mean ± SD. Experiments were repeated three times. *P < .05.

[39] and DDP chemoresistance [40], in tumors. In line with these reports, we observed that EBV-miR-BART22 activates the PI3K/AKT and GSK3β/β-catenin pathway and their downstream tumor stemness and EMT signals, which facilitated CSCs properties, metastasis, and chemoresistance of NPC cells.

To further explore the detailed molecular basis of EBV-miR-BART22 as a stimulator of tumor stemness and EMT signals, bioinformatics analysis was firstly used to predict MAP2K4 as the target of EBV-miR-BART22. Subsequently, we identified EBV-miR-BART22 directly targets MAP2K4 in NPC. Further, we used CoIP and mass

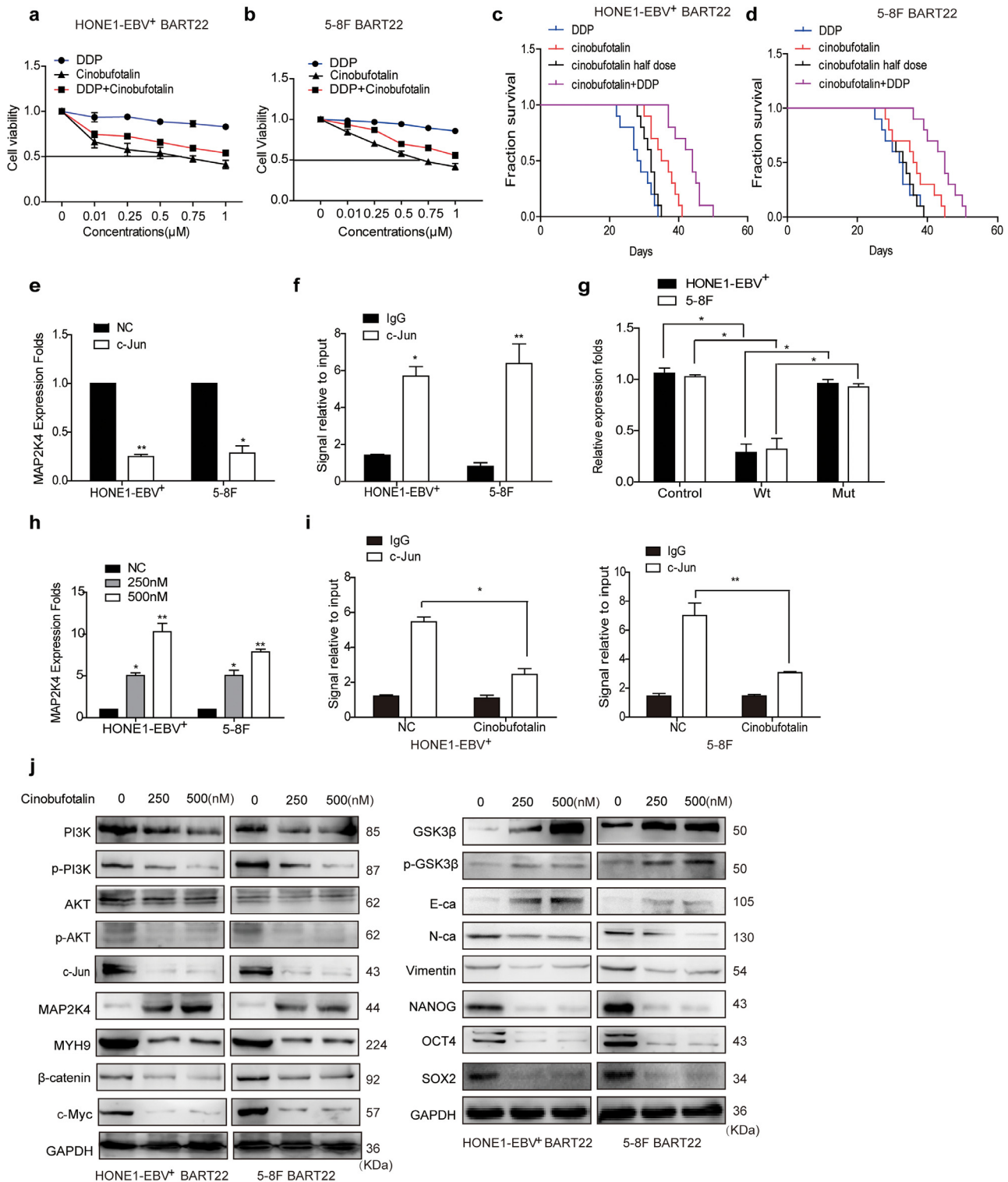


Fig. 6. Cinobufotalin reversed EBV-miR-BART22-induced DDP resistance by inducing the expression of MAP2K4. (a)(b) Dose-response curves of HONE1-EBV⁺ and 5-8F treated with miR-BART22 48 h after treatment with DDP, cinobufotalin or DDP combined with cinobufotalin. Parametric generalized linear model with random effects. (c)(d) Animals were divided into four groups: DDP, Cinobufotalin, Cinobufotalin with half dose, and DDP combined with Cinobufotalin (each group: N = 10). Survival analysis was plotted. Log-rank test ($P < .001$). (e) QPCR analysis of MAP2K4 mRNA levels in HONE1-EBV⁺ and 5-8F cells with c-Jun over-expressed or control (n = 3 independent experiments, Student's t-test). (f) ChIP analysis for c-Jun binding to the transcriptional regulatory region of MAP2K4 in HONE1-EBV⁺ and 5-8F cells. (g) Luciferase reporter assays (n = 3 independent experiments, one-way ANOVA) were performed to confirm that c-Jun stimulated the activation of the MAP2K4 promoter. (h) QPCR analysis of MAP2K4 mRNA levels in HONE1-EBV⁺ with cinobufotalin treated in 0.25, 0.5 μ M or control (n = 3 independent experiments, Student's t-test). (i) ChIP analysis for c-Jun binding to the transcriptional regulatory region of MAP2K4 in HONE1-EBV⁺ and 5-8F cells with cinobufotalin treatment. All data are presented as the mean \pm SD. Experiments were repeated three times. (j) Western blot analysis of PI3K, p-PI3K, AKT, p-AKT, c-Jun, MAP2K4, MYH9, β -catenin, c-Myc, GSK3 β , p-GSK3 β , E-cadherin, N-cadherin, Vimentin, Nanog, OCT4 and Sox2 expression in BART22-overexpressed NPC cells with cinobufotalin treatment in different dose.

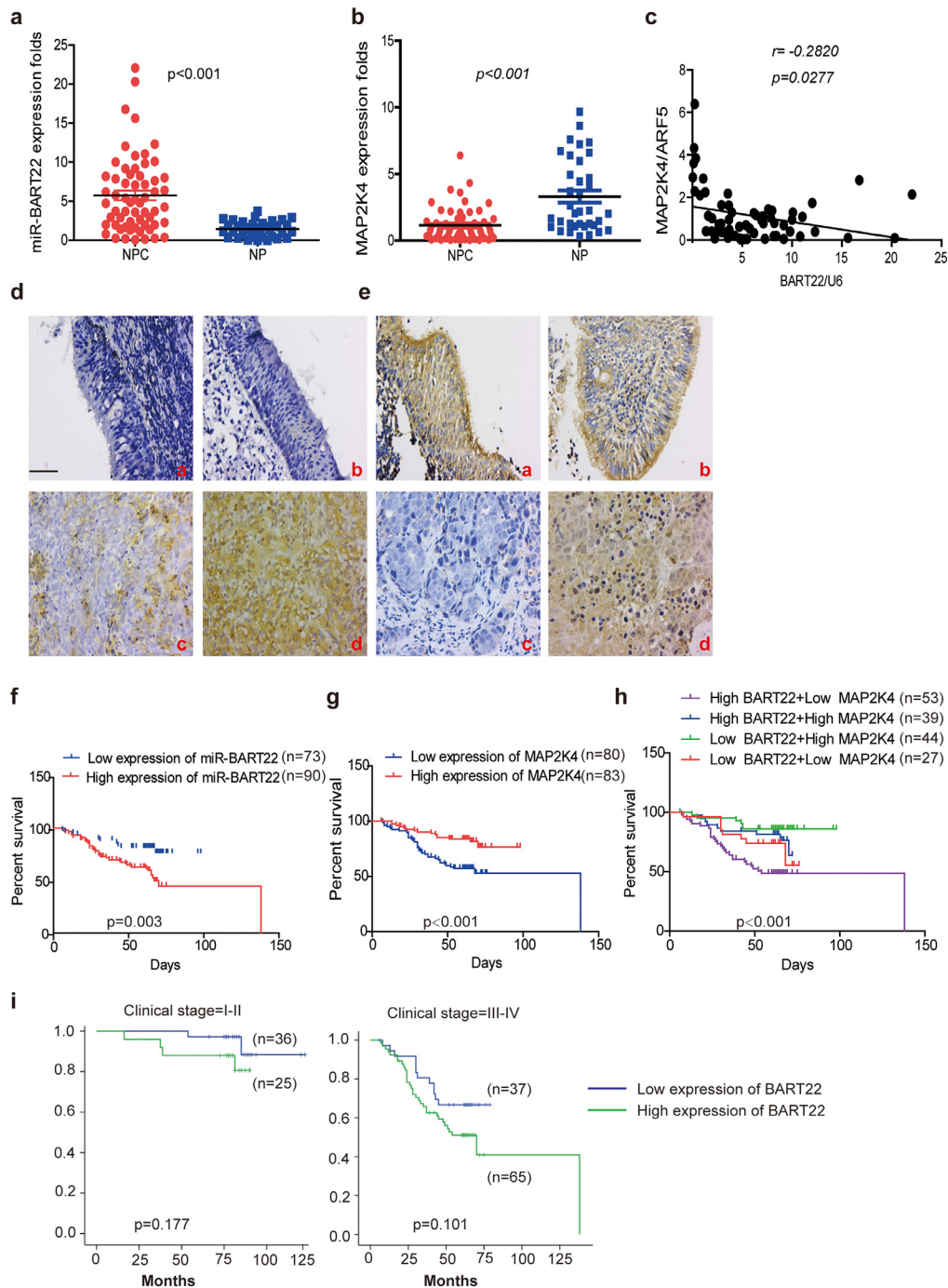


Fig. 7. Increased EBV-miR-BART22 and decreased *MAP2K4* expression in NPC.

(a)(b) The expression of EBV-miR-BART22 and *MAP2K4* in NP and NPC samples was determined by qRT-PCR. Student's t-test, mean \pm SD. (c) Correlations between miR-BART22 and *MAP2K4* expression levels were calculated. Two tailed Spearman's correlation analysis. Means \pm SD, $P = .0277$. (d) miR-BART22 expression in NP and NPC samples. (a)(b) Negative expression in NP tissues; (c) weak positive expression of miR-BART22 in NPC samples. (d) strong positive expression of miR-BART22 in NPC samples (original magnification $\times 400$, scale bar, $50 \mu\text{m}$). (e) *MAP2K4* expression in NP and NPC samples. (a)(b) strong staining of *MAP2K4* in NP samples. (c) Negative expression in NPC samples; (d) positive expression in NPC samples (original magnification $\times 400$, scale bar, $50 \mu\text{m}$). (f)(g) Kaplan-Meier survival analysis of overall survival of 163 NPC patients on the basis of miR-BART22 and *MAP2K4* expression. (log-rank test was used to calculate P values). (h) Kaplan-Meier survival analysis of overall survival in 163 NPC patients on the basis of low expression of miR-BART22 and high expression of *MAP2K4*. (log-rank test, $P < .001$). (i) Stratified analysis was used to analyze the correlation of the expression of miR-BART22 with survival prognosis in clinical stage(I-V) stage. (j) Stratified analysis was used to analyze the correlation of the expression of *MAP2K4* with survival prognosis in clinical stage(I-V) stage.

spectrometry to screen *MYH9* as the potential interacting protein with *MAP2K4* in NPC cells. Unfortunately, we did not detect the combination of *MYH9* with *MAP2K4* based on exogenous co-IP. Interestingly, we observed the downregulated *MYH9* mRNA and protein expression levels in *MAP2K4*-overexpressing NPC cells, which

suggested that *MAP2K4* suppressed the *MYH9* expression at the transcriptional level. In a previous study, c-Jun was reported to be an oncogenic transcription factor [41,42] that could bind to the *MYH9* promoter and transcriptionally upregulate *MYH9* mRNA expression. In a subsequent study, our data further revealed that

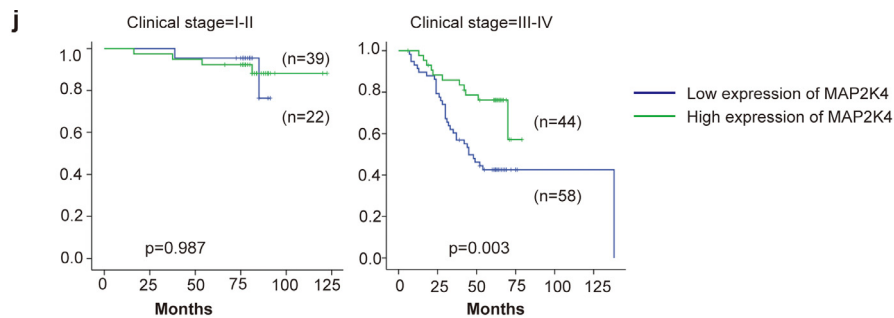


Fig. 7. Continued

c-Jun was a downstream positive factor of *PI3K/AKT* signal [43], which hinted that *MAP2K4* downregulated *MYH9* expression by suppressing *PI3K/AKT/c-Jun* signals and further reduced the combination of c-Jun and *MYH9* promoter. In subsequent investigation, we confirmed this speculation.

GSK3β inactivation stimulates the β -catenin-induced stemness and EMT signaling pathways and thus promotes CSC growth, metastasis, and chemoresistance in tumors [44,45]. Interestingly, we searched the DOMINE database and found that *GSK3β* was a potential protein binding to *MYH9*. Subsequently, *MYH9* was confirmed to bind to *GSK3β* and co-localized in cytoplasm of NPC. Furthermore, *MYH9* overexpression suppressed *GSK3β* protein expression, but not *GSK3β* mRNA level. We hypothesized that *MYH9* was involved in *GSK3β* protein ubiquitination degradation [46,47]. To confirm this speculation, we transfected NPC cells with an *MYH9* plasmid and observed that *GSK3β* ubiquitination was markedly increased in NPC. In addition, we interestingly observed that *MYH9* stimulated *PI3K/AKT/c-Jun* transcription to upregulate *ubiquitin* expression, which increased E3 ligase TRAF6 level to promote *GSK3β* ubiquitination and protein degradation. Finally, we confirmed that TRAF6-mediated *GSK3β* ubiquitination was greatly reduced when the K183R site of *GSK3β* is mutated [48]. Taken together, our data demonstrated that *MYH9* not only interacted with *GSK3β*, but also induced *ubiquitin* and *TRAF6* expression and further promoted *GSK3β* ubiquitin protein degradation, which thus activated β -catenin expression and its nuclear translocation in NPC. In a subsequent study, we observed that *MAP2K4* transduction or *MYH9* knockdown in miR-BART22 over-expression NPC cells significantly downregulated β -catenin-stimulated tumor stemness and EMT signals, and thus suppressed NPC tumor stemness formation, metastasis and DDP chemotherapy resistance. Altogether, these results confirmed that miR-BART22 is an oncogene that targets *MAP2K4* and further stimulates *MYH9*-mediated *GSK3β* ubiquitin protein degradation, which thus activates β -catenin and its downstream tumor stemness and EMT signaling pathways to promote tumor stemness formation, metastasis and chemotherapy resistance. Interestingly, *MYH9* had been shown to mediate EBV infection into nasopharyngeal epithelial cells as a receptor in previous document [49]. We speculated that EBV-encoded miR-BART22 can be secreted from NPC cells, which possibly enters into nasopharyngeal epithelial cells, induces *MYH9* expression via targeting *MAP2K4*, and ultimately stimulates EBV infection to nasopharyngeal epithelial cells. However, this idea is still to be determined.

Cinobufotalin is one of the bufadienolides prepared from toad venom with anticancer activity [50–52]. Pre-clinical studies showed that chemically synthesized cinobufotalin could induce cell death in lung cancer cells [33]. However, comparison of tumor cytotoxicity between cinobufotalin and DDP and their combined application for tumor treatment have never been reported. In this study, we initially observed that cinobufotalin markedly reduced

the IC50 value and significantly increased the DDP sensitivity to miR-BART22-overexpressing NPC cells. Further, using in vivo experiments for nude mice with injected miR-BART22-overexpressing NPC cells that simulated advanced NPC, we observed that cinobufotalin markedly prolonged the survival time of nude mice compared to those with the treatment of the same doses and administration time of DDP. More interestingly, we observed that the nude mice showed the longest survival times when cinobufotalin and DDP were used together compared with those that were treated with DDP or cinobufotalin alone. Mechanism analysis indicated that cinobufotalin induced *MAP2K4* expression by suppressing *PI3K/AKT/c-Jun* signaling and thus antagonized miR-BART22-induced *MYH9/GSK3β/β-catenin* and its downstream tumor stemness and EMT signaling, which has never been reported. Attributed to the fact that cinobufotalin induces chemosensitivity to DDP by stimulating *MAP2K4*, a downstream targeted gene of miR-BART22, to antagonize *MYH9/GSK3β/β-catenin* axis in miR-BART22-positive NPC cells, it may also reverse DDP chemoresistance via inducing *MAP2K4* in EBV-negative NPC cells, which is independent of EBV-miR-BART-22. These data suggested that cinobufotalin is a more promising anti-tumor agent than DDP in treating NPC. Furthermore, the coupled use of cinobufotalin and DDP may be a better choice for the treatment of miR-BART22-induced NPC chemoresistance.

In clinical samples, we observed that miR-BART22 was mainly expressed in NPC compared with nasopharyngeal epithelial (NP) tissues. In situ hybridization indicated that miR-BART22 was only expressed in NPC tissues. Increased miR-BART22 obviously promoted clinical progression and poor prognosis in NPC patients. Inversely, *MAP2K4* was predominantly expressed in NP tissues compared to NPC tissues. Reduced *MAP2K4* expression was negatively correlated with clinical progression and positively related to the overall survival time of NPC patients. Furthermore, miR-BART22 expression was negatively correlated with *MAP2K4* protein expression in NPC tissues. NPC patients with high miR-BART22 and low *MAP2K4* protein expression showed the worst survival prognosis compared to the other three group patients. These data demonstrated the significance of abnormal miR-BART22/*MAP2K4* signal in NPC pathogenesis.

Taken together, our study firstly revealed that EBV-miR-BART22 directly targets *MAP2K4* to stimulate *MYH9* expression, which thus induces *GSK3β* protein ubiquitin degradation and further promotes tumor stemness, metastasis and DDP chemotherapy resistance through activation of the β -catenin-stimulated stemness and EMT signaling pathways. Furthermore, we found that cinobufotalin could powerfully reverse EBV-miR-BART22-induced DDP resistance by inducing *MAP2K4* to antagonize *MYH9/GSK3β/β-catenin*-stimulated tumor stemness and EMT signals in nasopharyngeal carcinoma. Finally, the combination of increased miR-BART22 and reduced *MAP2K4* expression levels may be the significant marker to predict poor prognosis for NPC patients.

Funding sources

This study was supported by National Nature Science Fund of China (81772872, 81572643, 81872198), Science and Technology Project of Guangdong Province (No.2016A020215233, 20140212, 2014A020212342), People's Livelihood Science and Technology grant of Guangzhou Municipal Science and Technology project (No. 201803010023), Scientific research project of Guangdong Provincial Bureau of Traditional Chinese Medicine (No.20193010), Guangzhou Science and Technology plan(No.201804010023, 201707010425), Nature Science Fund of Guangdong Province (2016A030313526, 2017A030313701), The Supporting plan for Special Talents in Guangdong Province (No. 2016TQ03R466), Seeding program of Shenzhen Hospital of Southern Medical University, Guangdong Medical Science and Technology Research Fund Project (No.A2016610). The content is solely the responsibility of the authors and the funders did not have any role in study design, data collection, data analysis, interpretation, or writing of the report.

Authors' contributions

Conceptualization, Y.Y.L and W.Y.F; Methodology, Y.Y.L and W.Y.F; Investigation, Q.P.J, X.L, C.L, Z.B.T, M.Y.Z, J.Z, Z.C.X.L; Writing-Original Draft, Y.Y.L; Writing-Review & Editing, W.Y.F; Funding Acquisition, W.Y.F, Z.L, Q.P.J, J.Z, L.B.L, Y.Y.X; Resources, W.Y.F; Supervision, W.Y.F. All authors have read and approved the final manuscript.

Declaration of Competing Interest

Prof. Fang has a pending patent on Cinobufotalin (No. 201910399834.7). All authors declare that no support, financial or otherwise, has been received from any organization that may have an interest in the submitted work.

Acknowledgments

Not applicable.

Appendix A. Supplementary data

Supplementary data to this article can be found online at <https://doi.org/10.1016/j.ebiom.2019.08.040>.

References

- Bray F, Ferlay J, Soerjomataram I, Siegel RL, Torre LA, Jemal A. Global cancer statistics 2018: GLOBOCAN estimates of incidence and mortality worldwide for 36 cancers in 185 countries. *CA Cancer J Clin* 2018;68(6):394–424.
- Syn NL, Lim PL, Kong LR, Wang L, Wong AL, Lim CM, et al. Pan-CDK inhibition augments cisplatin lethality in nasopharyngeal carcinoma cell lines and xenograft models. *Signal Transduct Target Ther* 2018;3:9.
- Zhen Y, Fang W, Zhao M, Luo R, Liu Y, Fu Q, et al. miR-374a-CCND1-p13K/AKT-c-JUN feedback loop modulated by PDCD4 suppresses cell growth, metastasis, and sensitizes nasopharyngeal carcinoma to cisplatin. *Oncogene*. 2017;36(2):275–85.
- Ren X, Yang X, Cheng B, Chen X, Zhang T, He Q, et al. HOPX hypermethylation promotes metastasis via activating SNAIL transcription in nasopharyngeal carcinoma. *Nat Commun* 2017;8:14053.
- Smith C. EBV and nasopharyngeal carcinoma: a target for cellular therapies. *Immunotherapy*. 2013;5(8):821–4.
- Liang Z, Liu Z, Cheng C, Wang H, Deng X, Liu J, et al. VPS33B interacts with NESG1 to modulate EGFR/PI3K/AKT/c-Myc/P53/miR-133a-3p signaling and induce 5-fluorouracil sensitivity in nasopharyngeal carcinoma. *Cell Death Dis* 2019;10(4):305.
- Lo KW, To KF, Huang DP. Focus on nasopharyngeal carcinoma. *Cancer Cell* 2004;5(5):423–8.
- Cohen JL. Epstein-Barr virus infection. *N Engl J Med* 2000;343(7):481–92.
- Hu L, Lin Z, Wu Y, Dong J, Zhao B, Cheng Y, et al. Comprehensive profiling of EBV gene expression in nasopharyngeal carcinoma through paired-end transcriptome sequencing. *Front Med* 2016;10(1):61–75.
- Young LS, Yap LF, Murray PG. Epstein-Barr virus: more than 50 years old and still providing surprises. *Nat Rev Cancer* 2016;16(12):789–802.
- Chua MLK, Wee JTS, Hui EP, Chan ATC. Nasopharyngeal carcinoma. *Lancet*. 2016;387(10022):1012–24.
- Yachi K, Tsuda M, Kohsaka S, Wang L, Oda Y, Tanikawa S, et al. miR-23a promotes invasion of glioblastoma via HOXD10-regulated glial-mesenchymal transition. *Signal Transduct Target Ther* 2018;3:33.
- Ma M, Dai J, Tang H, Xu T, Yu S, Si L, et al. MicroRNA-23a-3p inhibits mucosal melanoma growth and progression through targeting adenylate cyclase 1 and attenuating cAMP and MAPK pathways. *Theranostics*. 2019;9(4):945–60.
- Fu Q, Song X, Liu Z, Deng X, Luo R, Ge C, et al. miRNomics and proteomics reveal a miR-296-3p/PRKCA/FAK/Ras/c-Myc feedback loop modulated by HDGF/DDX5/beta-catenin complex in Lung adenocarcinoma. *Clin Cancer Res* 2017;23(20):6336–50.
- Deng X, Liu Z, Liu X, Fu Q, Deng T, Lu J, et al. miR-296-3p Negatively Regulated by Nicotine Stimulates Cytoplasmic Translocation of c-Myc via MK2 to Suppress Chemotherapy Resistance. *Mol Ther*. 2018;26(4):1066–81.
- Cosmopoulos K, Pegtel M, Hawkins J, Moffett H, Novina C, Middeldorp J, et al. Comprehensive profiling of Epstein-Barr virus microRNAs in nasopharyngeal carcinoma. *J Virol* 2009;83(5):2357–67.
- Lo AK, Dawson CW, Jin DY, Lo KW. The pathological roles of BART miRNAs in nasopharyngeal carcinoma. *J Pathol* 2012;227(4):392–403.
- Coghill AE, Bu W, Nguyen H, Hsu WL, Yu KJ, Lou PJ, et al. High levels of antibody that neutralize B-cell infection of Epstein-Barr virus and that bind EBV gp350 are associated with a lower risk of nasopharyngeal carcinoma. *Clin Cancer Res* 2016;22(14):3451–7.
- Zhao CX, Zhu W, Ba ZQ, Xu HJ, Liu WD, Zhu B, et al. The regulatory network of nasopharyngeal carcinoma metastasis with a focus on EBV, lncRNAs and miRNAs. *Am J Cancer Res* 2018;8(11):2185–209.
- Cai L, Ye Y, Jiang Q, Chen Y, Lyu X, Li J, et al. Epstein-Barr virus-encoded microRNA BART1 induces tumour metastasis by regulating PTEN-dependent pathways in nasopharyngeal carcinoma. *Nat Commun* 2015;6:7353.
- Zhang G, Zong J, Lin S, Verhoeven RJ, Tong S, Chen Y, et al. Circulating Epstein-Barr virus microRNAs miR-BART7 and miR-BART13 as biomarkers for nasopharyngeal carcinoma diagnosis and treatment. *Int J Cancer* 2015;136(5):E301–12.
- Jiang QP, Liu SY, He XF, Peng J, Xiong HZ, Xiong ZT, et al. Relationship between MAP3K5 and Epstein-Barr virus-encoded miR-BART22 expression in nasopharyngeal carcinoma. *Nan Fang Yi Ke Da Xue Xue Bao* 2011;31(7):1146–9.
- Lung RW, Tong JH, Sung YM, Leung PS, Ng DC, Chau SL, et al. Modulation of LMP2A expression by a newly identified Epstein-Barr virus-encoded microRNA miR-BART22. *Neoplasia*. 2009;11(11):1174–84.
- Zhao C, Gomez GA, Zhao Y, Yang Y, Cao D, Lu J, et al. ETV2 mediates endothelial transdifferentiation of glioblastoma. *Signal Transduct Target Ther* 2018;3:4.
- Boso D, Rampazzo E, Zanon C, Bresolin S, Maule F, Porcù E, et al. HIF-1 α /Wnt signaling-dependent control of gene transcription regulates neuronal differentiation of glioblastoma stem cells. *Theranostics* 2019;9(17):4860–77.
- Chen HJ, Huang RL, Liew PL, Su PH, Chen LY, Weng YC, et al. GATA3 as a master regulator and therapeutic target in ovarian high-grade serous carcinoma stem cells. *Int J Cancer* 2018;143(12):3106–19.
- Wu CX, Wang XQ, Chok SH, Man K, Tsang SHY, Chan ACY, et al. Blocking CDK1/PDK1-Catenin signaling by CDK1 inhibitor RO3306 increased the efficacy of sorafenib treatment by targeting cancer stem cells in a preclinical model of hepatocellular carcinoma. *Theranostics*. 2018;8(14):3737–50.
- Lin MC, Chen SY, He PL, Herschman H, Li HJ. PGE2/EP4 antagonism enhances tumor chemosensitivity by inducing extracellular vesicle-mediated clearance of cancer stem cells. *Int J Cancer* 2018;143(6):1440–55.
- Bi QR, Hou JJ, Qi P, Ma CH, Shen Y, Feng RH, et al. Venenum Bufonis induces rat neuroinflammation by activating NF-kappaB pathway and attenuation of BDNF. *J Ethnopharmacol* 2016;186:103–10.
- Nogawa T, Kamano Y, Yamashita A, Pettit GR. Isolation and structure of five new cancer cell growth inhibitory bufadienolides from the Chinese traditional drug Ch'an Su. *J Nat Prod* 2001;64(9):1148–52.
- Dong Y, Yin S, Li J, Jiang C, Ye M, Hu H. Bufadienolide compounds sensitize human breast cancer cells to TRAIL-induced apoptosis via inhibition of STAT3/Mcl-1 pathway. *Apoptosis* 2011;16(4):394–403.
- Xie CM, Chan WY, Yu S, Zhao J, Cheng CH. Bufalin induces autophagy-mediated cell death in human colon cancer cells through reactive oxygen species generation and JNK activation. *Free Radic Biol Med* 2011;51(7):1365–75.
- Meng Z, Yang P, Shen Y, Bei W, Zhang Y, Ge Y, et al. Pilot study of huachansu in patients with hepatocellular carcinoma, nonsmall-cell lung cancer, or pancreatic cancer. *Cancer*. 2009;115(22):5309–18.
- Kai S, Lu JH, Hui PP, Zhao H. Pre-clinical evaluation of cinobufotalin as a potential anti-lung cancer agent. *Biochem Biophys Res Commun* 2014;452(3):768–74.
- Ko R, Park JH, Ha H, Choi Y, Lee SY. Glycogen synthase kinase 3beta ubiquitination by TRAF6 regulates TLR3-mediated pro-inflammatory cytokine production. *Nat Commun* 2015;6:6765.
- Nepstad I, Hatfield KJ, Grønningsæter IS, Aasebo E, Hernandez-Valladares, M, Hagen KM. Effects of insulin and pathway inhibitors on the PI3K-Akt-mTOR phosphorylation profile in acute myeloid leukemia cells. *Signal Transduct Target Ther*. 2019;4:20.
- Pan J, Fan Z, Wang Z, Dai Q, Xiang Z, Yuan F, et al. CD36 mediates palmitate acid-induced metastasis of gastric cancer via AKT/GSK-3beta/beta-catenin pathway. *J Exp Clin Cancer Res* 2019;38(1):52.
- Fregni G, Quinodoz M, Moller E, Vuille J, Galland S, Fusco C, et al. Reciprocal modulation of mesenchymal stem cells and tumor cells promotes lung cancer metastasis. *EBioMedicine*. 2018;29:128–45.

- [39] Feng YF, Lei YY, Lu JB, Xi SY, Zhang Y, Huang QT, et al. RIT1 suppresses esophageal squamous cell carcinoma growth and metastasis and predicts good prognosis. *Cell Death Dis* 2018;9(11):1085.
- [40] Lu H, Ju DD, Yang GD, Zhu LY, Yang XM, Li J, et al. Targeting cancer stem cell signature gene SMOC-2 overcomes chemoresistance and inhibits cell proliferation of endometrial carcinoma. *EBioMedicine*. 2019;40:276–89.
- [41] Eferl R, Wagner EF. AP-1: a double-edged sword in tumorigenesis. *Nat Rev Cancer* 2003;3(11):859–68.
- [42] Guan PP, Ding WY, Wang P. The roles of prostaglandin F2 in regulating the expression of matrix metalloproteinase-12 via an insulin growth factor-2-dependent mechanism in sheared chondrocytes. *Signal Transduct Target Ther* 2018;3:27.
- [43] Zhao M, Luo R, Liu Y, Gao L, Fu Z, Fu Q, et al. miR-3188 regulates nasopharyngeal carcinoma proliferation and chemosensitivity through a FOXO1-modulated positive feedback loop with mTOR-p-PI3K/AKT-c-JUN. *Nat Commun* 2016;7:11309.
- [44] Yu J, Liu D, Sun X, Yang K, Yao J, Cheng C, et al. CDX2 inhibits the proliferation and tumor formation of colon cancer cells by suppressing Wnt/beta-catenin signaling via transactivation of GSK-3beta and Axin2 expression. *Cell Death Dis* 2019;10(1):26.
- [45] Li B, Cao Y, Meng G, Qian L, Xu T, Yan C, et al. Targeting glutaminase 1 attenuates stemness properties in hepatocellular carcinoma by increasing reactive oxygen species and suppressing Wnt/beta-catenin pathway. *EBioMedicine*. 2019;39:239–54.
- [46] Suber T, Wei J, Jacko AM, Nikolli I, Zhao Y, Zhao J, et al. SCF(FBXO17) E3 ligase modulates inflammation by regulating proteasomal degradation of glycogen synthase kinase-3beta in lung epithelia. *J Biol Chem* 2017;292(18):7452–61.
- [47] Teixeira FR, Randle SJ, Patel SP, Mevissen TE, Zenkeviciute G, Koide T, et al. Gsk3beta and Tomm20 are substrates of the SCFFbxo7/PARK15 ubiquitin ligase associated with Parkinson's disease. *Biochem J* 2016;473(20):3563–80.
- [48] Yoon K, Jung EJ, Lee SR, Kim J, Choi Y, Lee SY. TRAF6 deficiency promotes TNF-induced cell death through inactivation of GSK3beta. *Cell Death Differ* 2008;15(4):730–8.
- [49] Xiong D, Du Y, Wang HB, Zhao B, Zhang H, Li Y, et al. Nonmuscle myosin heavy chain IIa mediates Epstein-Barr virus infection of nasopharyngeal epithelial cells. *Proc Natl Acad Sci U S A* 2015;112(35):11036–41.
- [50] Emam H, Zhao QL, Furusawa Y, Refaat A, Ahmed K, Kadowaki M, et al. Apoptotic cell death by the novel natural compound, cinobufotalin. *Chem Biol Interact* 2012;199(3):154–60.
- [51] Cheng L, Chen YZ, Peng Y, Yi N, Gu XS, Jin Y, et al. Ceramide production mediates cinobufotalin-induced growth inhibition and apoptosis in cultured hepatocellular carcinoma cells. *Tumour Biol* 2015;36(8):5763–71.
- [52] Jing Y, Ohizumi H, Kawazoe N, Hashimoto S, Masuda Y, Nakajo S, et al. Selective inhibitory effect of bufalin on growth of human tumor cells in vitro: association with the induction of apoptosis in leukemia HL-60 cells. *Jpn J Cancer Res* 1994;85(6):645–51.